Shear Wave Seismic Interferometry for Lithospheric Imaging

Jordan G. Frank

June 25, 2013

Shear Wave Seismic Interferometry for Lithospheric Imaging

Developing a new imaging technique with an application in southern Mexico

Abstract

Green's function retrieval by seismic interferometry (SI) exists in a variety of forms. Many of the applications of SI allow the creation of new seismic traces by crosscorrelating a wavefield recorded at two separate locations. The sum of this operation over multiple sources results in the creation of a new signal such that one of the recording locations acts as a virtual source to the other. We demonstrate that it is possible to use teleseismic shear wave transmission responses to create virtual source records for lithospheric imaging through SI. We utilize teleseismic shear wave phases for primarily two reasons: namely, (a) at large offsets the incoming wavefront approximates a plane wave due to spread of the wavefront in relation to the comparatively finite seismic array, and (b) the large distances act as a natural temporal filter to separate the incident P and S arrivals. We develop a method that allows such shear wave phases to image the subsurface.

A series of forward modelling experiments with 2D elastic propagation were conducted. SP converted energy maps primarily to the vertical component. At large ray parameters, decomposition was capable of separating the P and S fields. Sufficient illumination by many ray parameters is essential to clearly resolve subsurface features; however, decimation studies indicated that it is still possible to identify strong reflectors with suboptimal sampling. Attempts to mitigate the complex effective wavelet generated by earthquake faulting behaviour were met with difficulty; deconvolution was unsuccessful due to the non-minimum phase nature of the effective source wavelet, but spectral whitening is a necessary preprocessing step to SI was necessary. Correlation panel filtering techniques, including singular value decomposition and wavenumber filtering, were tested to remove spurious energy present in the virtual source records created through SI. Spurious terms introduced by the long duration earthquake-generated wavelet were further suppressed in the common-offset domain. After creating virtual source records at every model receiver location, imaging was performed. A conventional migration technique was applied to each virtual source record and stacked to produce an image of the model subsurface. All major features of the model were resolved with a high degree of accuracy using the approach developed here.

Finally, a field dataset was selected from southern Mexico with sufficient S phase sampling and prepared for imaging. By azimuthally limiting a window around the relatively linear orientation of the seismometer array, earthquakes that vary in distance correspond to sampling of unique ray parameters. A total of 43 S phase transmission responses were selected that met our criteria for magnitude and location. Geometric and topographic corrections were applied to each transmission response. The processing steps tested on our forward models were subsequently applied to this dataset and virtual source records were created via SI. The virtual source records are then

migrated to form an image of the lithosphere. The resulting image of the Cocos subduction zone reproduces features present in the literature and also reveals new details at greater depths; this demonstrates the utility of the method developed within.

Acknowledgements

I would like to thank Professor Evert Slob for introducing me to the project that is discussed in this thesis. Without his involvement, I would not have been brought into the TU Delft environment to work on this exciting subject. Without the direct supervision of Doctor Elmer Ruigrok and the resources made freely available by him, this project would not have succeeded to the degree that it has. The concept for this project was established by Elmer previously, and I am grateful for his continuous guidance and direct interest in all facets of this work. Professor Kees Wapenaar offered his insight and direction on many occasions throughout the previous year. I sincerely appreciate the time and effort he has provided to ensure a successful project. Both Elmer and Professor Wapenaar were essential in ensuring this work received a wider exposure at the American Geophysical Union's 2013 Meeting of the Americas; this conference experience made the thesis effort all the more rewarding. Furthermore, the research environment and presence of other dedicated staff at TU Delft have made this year a positive, and memorable, journey.

On a personal note, I would like to thank my family for all of their support while I spent two years living abroad, halfway around the globe. Loving parents and supportive siblings have made the distance appear negligible despite thousands of kilometres between. I am grateful for the foundation my parents have raised me on and I fully appreciate that any achievements that may be accomplished under my name are not fully my own, but are rather the product of the influences that have shaped me the most. A last note must be made in dedication to my loving fiancée; her patience and understanding while I adventured around the European continent will not be forgotten.

Contents

Chapter 1

Introduction

The objective of this project is two fold: first, to develop a new technique for lithospheric imaging through the implementation of seismic interferometry (SI), and second, to apply this method to a field dataset. To achieve the first objective, a discussion of SI is necessary. It is established that SI exists in a variety of mathematical forms to address a variety of applications. Many of the uses of SI centre on the ability to create new seismic traces by crosscorrelating a received signal recorded at separate locations. The sum of this operation for multiple sources is the creation of a new signal such that one of the recording locations acts as a virtual source to the remaining receiver. This mechanism and related theory are described in detail in Wapenaar et al. (2010). With many receiver positions available on a free surface, it is possible to produce reflection responses as if sources were present at one of the receiver locations on the surface. For a situation where a distribution of receivers is located on the surface of the earth, it is feasible that virtual source records, similar to those produced by conventional seismic experiments, may be created. Determining the best practise for creating these virtual source records from the recordings of distant earthquake events is the first component of the problem. Applying SI to create a series of virtual source records and applying migration to the results is next required. This process is discussed in detail in the following chapters; the theory is discussed, simple 1D models are created and treated, and the method is established on a 2D model designed to include features anticipated in a subduction setting.

The second objective is fairly straightforward; we wish to image a portion of the subduction zone beneath southern Mexico. To produce an image of the Cocos subduction beneath southern Mexico, a dataset is selected with sufficient surface coordinate sampling and plentiful earthquake recordings. The Meso American Subduction Experiment (MASE) array spans over five hundred linear kilometres from Acapulco on the southern coast toward the town of Tempoal in the north. With 100 receiver stations spaced at approximately 5 km intervals, sufficient station spacing for the purpose of imaging is achieved. Previous studies in the region focus on the use of receiver functions (Pérez-Campos et al., 2008) and tomography (Husker and Davis, 2009) to draw conclusions regarding the structure of the subsurface. While useful for illustrating the subduction zone setting, both techniques have their respective flaws. Receiver functions, by definition of the theory employed, struggle to image non-horizontal subsurface features. In a subduction zone (particularly the steeply dipping Cocos plate), this causes difficulty once dip exceeds a certain

threshold. Tomographic inversion offers imaging capabilities to greater depth (independent of dip), but suffers from large grid sizes and the need to impose boundary conditions to constrain model results. The size of the grid is proportional to resolution, yet grid dimensions must be selected such that sufficient sampling is available within each bin. The technique developed here is unique in that the image reveals reflectivity directly; unlike tomography or receiver functions, which depend on velocity anomalies or convertibility, respectively. We intend to achieve sufficient sampling of the subsurface by using shear phases from teleseismic earthquake events as the imaging source. Here, teleseismic events refers to seismic events originating at greater than 30° epicentral distance. By developing a theory that allows the arriving wave front to be approximated by a plane wave, it is possible to create virtual source records via SI with sufficient ray parameter sampling. A similar method has been established for P wave recordings in Ruigrok et al. (2010).

Furthermore, the Mexican subsurface is an intriguing area to apply a new imaging technique. The complex subsurface is composed of horizontally migrating slabs, extensive tears and changes of dip along the Cocos plate, non-volcanic tremors, regions of high seismic attenuation, and areas of earthquakes and volcanism surrounding heavily populated portions of the country (Payero et al. (2008); Pérez-Campos et al. (2008); Chen and Clayton (2009); Husker and Davis (2009); Contreras-Reyes et al. (2012)). Although the MASE dataset has been publicly available for a number of years, there are still mysteries that remain to be solved. Additionally, there are regions very near the array location that appear to be storing significant seismic stress; while many of the surrounding regions have experienced earthquakes within recent history, some areas along the coast of southern Mexico are notably absent of such seismicity (Ramírez-Herrera et al., 2009). When this stress is inevitably released, the consequences will be significant to the population. Understanding the lithosphere in this area of the world is valuable; although the research presented here may not directly impact the quality of human life immediately, improvements in imaging capabilities (regardless of the scientific field) nearly always impacts other facets of human endeavour.

Chapter 2

Theory

We begin discussing the theoretical foundation for the technique in development. Shear waves are desirable for imaging due to the relatively low velocity with which they propagate through the lithosphere, an increased sensitivity to melt, and the potential for separate treatment of the S_V and S_H fields. We select earthquakes at teleseismic distances for primarily two reasons: (a) at large offsets the incoming energy approximates a plane wave due to the spread of the wavefront in relation to the comparatively finite seismic array, and (b) long epicentral offsets act as a natural temporal filter to separate the incident P and S arrivals. We also anticipate benefiting from the unique ray parameters sampled by each of the various S phases (i.e. S, SS, ScS, PS, and SKS). Practical obstacles include the complex source time function of earthquake events and imperfect techniques for distilling the S and P fields present at the receiver. We attempt to mitigate these obstacles through the implementation of deconvolution, spectral whitening, and receiver side decomposition.

We begin with the elastic Green's function representation that provides the basis for this work: from Draganov et al. (2006), we reprint

$$G^{\upsilon,\tau}_{p,q}(\mathbf{x}_A,\mathbf{x}_B,t)+G^{\upsilon,\tau}_{p,q}(\mathbf{x}_A,\mathbf{x}_B,-t)\approx\frac{2}{\rho c^K}\int_{\partial D_1}G^{\upsilon,\phi}_{p,K}(\mathbf{x}_A,\mathbf{x},t)*G^{\upsilon,\phi}_{q,K}(\mathbf{x}_B,\mathbf{x},-t)d^2\mathbf{x}. \quad (2.1)$$

The left hand side of the equation represents the retrieved Green's function in terms of particle velocity (υ) due to an impulsive traction source (τ) at the surface; both the causal and acausal (time-reversed) responses are retrieved. Einstein's summation convention applies to Latin subscripts. Here, subscript p represents the direction of particle velocity of the received response at $\mathbf{x}_A$ due to a traction source in the direction of subscript q at position $\mathbf{x}_B$. For the retrieved Green's function, both the receivers and sources are located on the free surface. Note that the derivation in Draganov et al. (2006) expands on previous work by Wapenaar and Fokkema (2006) where approximations, primarily regarding amplitude, are employed. The right hand side Green's functions represent the particle velocity observations due to an impulsive source at $\mathbf{x}$; $\mathbf{x}$ denotes a location on ∂D_1, which spans an open boundary in the subsurface. Here, ϕ repre-

sents a P-wave source when $K = 0$ or S-wave source polarizations for $K = 1, 2, 3$. Similarly, c^K represents the propagation velocity of the corresponding wave, and ρ represents the density.

We intend to utilize equation 2.1 for a scenario where plane wave transmission responses (the right hand side of the equation) from the subsurface are used to retrieve a reflection response from receivers on the surface (the left hand side of the equation). For the purposes of this project, we apply further approximations to equation 2.1 with the goal of representing the two shear wavefields (S_V and S_H) as independent scalar fields. As mentioned previously, for teleseismic sources the earth acts as a temporal filter for separating the incident P and S energy due to the differences in propagation velocity. By the time the S wave arrives, any remaining P wave energy is greatly attenuated compared to the energetic S arrival. Thus the primary contribution of P energy remaining in the system is from SP mode conversions. For low ray parameters, the P, S_V, and S_H fields map primarily to the vertical, radial, and transverse components, respectively. Large ray parameters require decomposition to isolate the S_V contribution; larger angles of incidence at an interface generally increases the amount of S to P conversion. By selecting seismic events within a narrow azimuthal range along the trend of the seismometer array and receiving near-planar wavefields, we apply a 2D approximation to equation 2.1. We further rewrite the expression to accommodate the transition from point sources to plane-wave sources (Ruigrok et al., 2010) and formulate the S_V expression as

$$G_{S_V}(\mathbf{x}_B, \mathbf{x}_A, t) + G_{S_V}(\mathbf{x}_B, \mathbf{x}_A, -t) \propto \int_{\partial S_1} G_{S_V}(\mathbf{x}_B, p, t) * G_{S_V}(\mathbf{x}_A, p, -t) dp, \tag{2.2}$$

where p is the incident ray parameter and ∂S_1 is a scalar distribution of ray parameters. Note that this scalar approximation does not account for SP converted energy that may be converted back to S waves. Mode converted SP energy is typically low in comparison to dominant S wave amplitude, so any energy present through subsequent PS conversion may be neglected. A similar formulation in terms of the S_H field may also be created; in this case, an added benefit is that mode converted energy is not present in the horizontally polarized field.

In order to produce an image through conventional processing means, virtual source records are produced via SI. The argument of the right hand side of equation 2.2 (and it's S_H analogue) represent the transmission responses of earthquake S phases recorded at the receiver array. In practise, the integral is not continuous; rather, discrete transmission responses are available within a given dataset. With sufficient sampling, a virtual source record may be produced. As depicted in figure 2.1, multiple ray parameters may be sampled with a single earthquake through the generation of multiple S phases; this is particularly true of large magnitude earthquakes with significant amplitude. We intend to use both S_V and S_H components in our method. We do not treat the dataset for anisotropy effects as the impact is anticipated to be negligible over the low frequency band that will be encountered for lithospheric imaging. Therefore, combining the S_V and S_H transmission responses as input to SI proceeds without distinguishing between the two.

With the virtual source records produced for all surface receiver locations, we proceed to the imaging stage. Conventional imaging techniques may be applied at this stage as the records produced are indistinguishable from conventional seismic records with the exception that surface waves are not created by the SI method employed. The practical aspects of the above theory are discussed in the subsequent chapters.

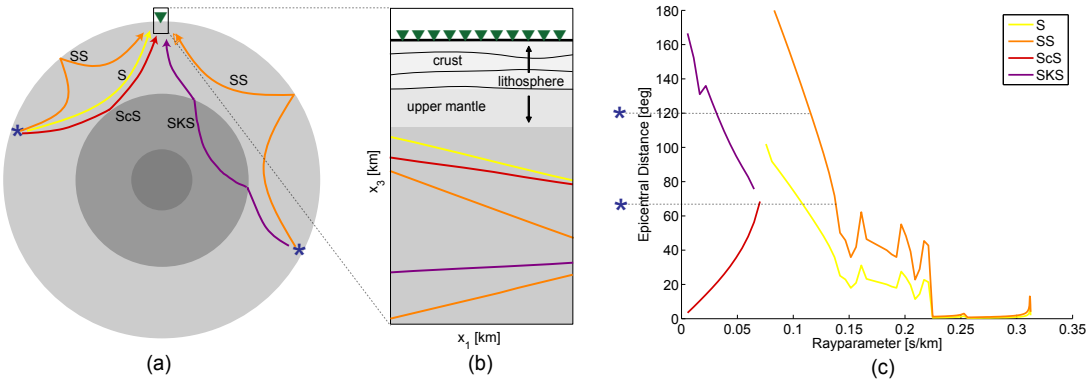

Figure 2.1: Panel (a) depicts the generation of multiple S phases from single earthquakes. Panel (b) depicts the sampling of unique ray parameters by the individual phases. Panel (c) demonstrates the relationship between epicentral distance an possible ray parameter sampling.

Chapter 3

1D Modelling

3.1 The Model

The model created consists of a 1D layered earth with 2D elastic wave propagation. Significant density and velocity contrasts were introduced at depths of 15 km and 40 km, overlaying a homogeneous halfspace. A series of 2C receivers (vertical and radial components) were defined along the surface at a spacing of 500 m for a total of 50 km (Figure 3.1). A planar S-wave source illuminates the model ray parameter sampling from -0.120 s/km to 0.120 s/km at every 0.005 s/km, yielding a total of 49 unique ray parameters. The source wavelet is a first order derivative of a Gaussian function with dominant and maximum frequencies of 0.5 Hz and 1.0 Hz, respectively. In the previous section, figure 2.1 illustrates how the configuration in the modelling experiment is similar to the expected field scenario; a similar approach has been followed with P phases in Ruigrok et al. (2010). Note that teleseismic events preferentially contribute to the lower end of possible ray parameters.

3.2 Decomposition

For the purpose of our technique, we need to isolate shear wave energy within the system. As predicted by Snell's law, ray paths deviate toward vertical when propagating from a high to low velocity. The lower velocities present below the receiver array implies that over the range of ray parameters investigated, wave arrivals at the receiver positions bias toward vertical orientation. This results in the majority of the S energy mapping to the radial component with mode converted SP energy mapping primarily to the vertical component. In order to further separate the P and S energy a series of decomposition experiments were conducted according to the method outlined in Kennett (1991). When decomposition was applied to individual shot records, mode converted P energy was diminished in the S_V recording by about an order of magnitude (in terms of maximum amplitude). This minimized, but consistent, SP converted energy across the individual records is likely to map to the SI output. Since the decomposition process still contributes to a cleaner

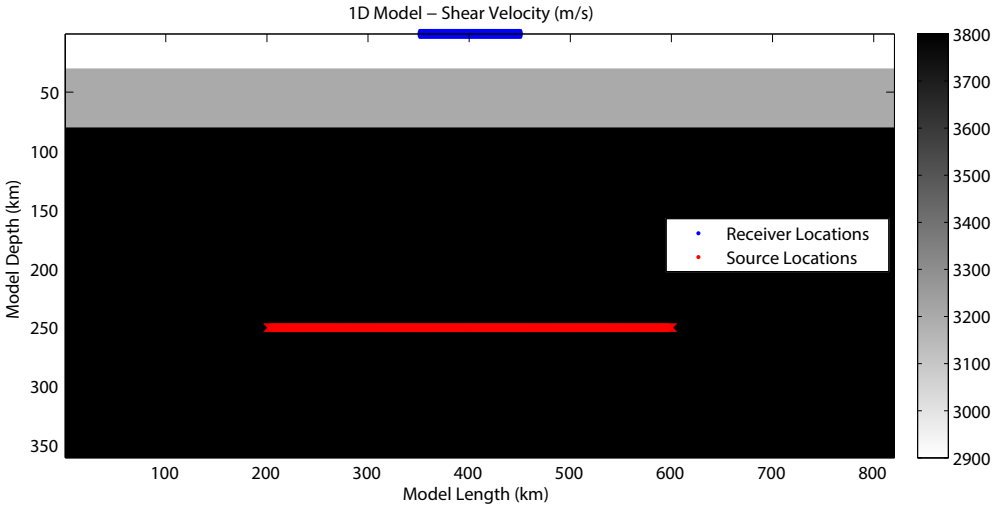

Figure 3.1: The 1D model in terms of shear wave velocity. Receiver and source positions are highlighted; material property contrasts are located at 15 km and 40 km depths.

S_V response, we proceed with the decomposed dataset for the 1D model. A further discussion of decomposition occurs for the 2D model in the following section (Chapter 4).

3.3 SI

Next, SI (as described in equation 2.2) is applied to the decomposed dataset. Figure 3.2 compares the SI result generated by treating the central receiver position as the virtual source location with a reference shot record from the same position. Reflections are named with the first letter representing the downgoing field, the second letter representing the upgoing field, and numerical subscript describes the reflection interface (interface 1 at 15 km and interface 2 at 40 km). Using well sampled synthetic data led to an SI result that clearly reproduces the primary reflections in addition to multiples and mode conversions from the interfaces. There are trace levels of undesirable reflections present in the output that correspond to spurious cross terms of various S and P events; it is possible that further processing techniques could be implemented to reduce this effect, but such finessing is not the focus of this section given the minimized appearance of these artifacts.

The reference response in figure 3.2 shows the horizontal particle velocity recording due to an S wave source placed at the centre of the receiver array. Due to the source definition in FDELMODC (the forward modelling program), taking the derivative of the reference model is required to match the phase of the SI result (Thorbecke and Draganov, 2011). As we aim to retrieve the S wave response from an S wave source via SI, we expect a small mismatch in amplitude between the reference and SI response. Moreover, SP converted energy will be present in the reference response, at long offsets, but should not be present in a retrieved response with decomposition applied. Shallow events at long offsets are not reproduced exactly due to the lack of large ray parameters in the SI input. Since surface waves are not present in the plane wave transmissions used as input to SI, they are not reproduced in the virtual source record; however, they are present in the reference response. It is worth observing that one of the approximations

stated for deriving equation 2.2, which claims the SP converted energy is expected to be negligible, may not be true; there is still some amount of SP energy interacting within the record. This converted energy could be eliminated by carrying over crosscorrelations of P wave responses from equation 2.1 and subtracting them from the system. However, the presence of this small amount of SP converted energy is not a significant detriment to the virtual source record.

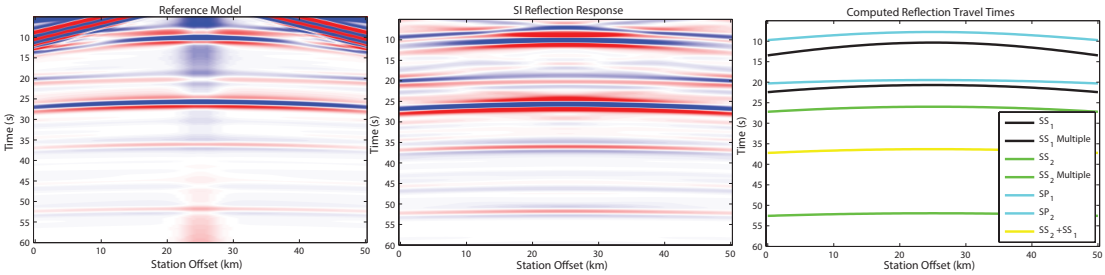

Figure 3.2: Comparison of the reference reflection record (left) with SI reflection record (centre). Note that amplitudes are clipped to improve visual clarity in both panels. Arrival times of significance are computed and compared on the right.

Off-Centre SI

A few SI results were computed for a virtual source located at the edge of the profile. In this case, the first receiver position was used as the virtual source location (Figure 3.3); as may have been expected, SI performs well even at long offsets in the simple 1D case. With the absence of any surface waves and direct arrivals in the SI result, the image is clearer than the reference case.

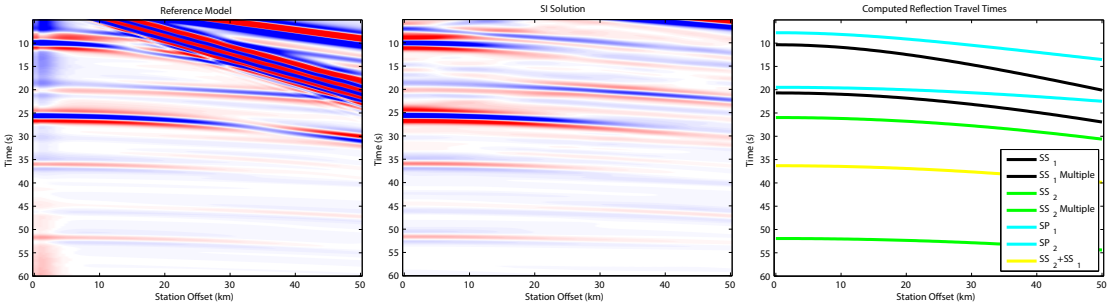

Figure 3.3: Comparison of the reference reflection model (left) with SI reflection response (centre) for a virtual source at the edge of the profile. Note that amplitudes are clipped to improve visual clarity in both panels. Arrival times of significance are computed and compared on the right.

3.4 Decimation Study

By decimating the number of unique plane wave ray parameters we determine the ability of the SI method to accurately reconstruct a seismic record from a sparsely sampled dataset. The reality of the physical world is that data is often not available uniformly sampled, therefore

determining what level of sampling is required to achieve a suitable result is valuable. In order to test the SI method in this capacity, the total aperture of the ray parameters is held constant, but the availability of ray parameters within the aperture is reduced. As mentioned in the previous section, the 1D dataset contained ray parameters from -0.120 s/km through +0.120 s/km at intervals of 0.005 s/km for a total of 49 unique ray parameters. In order to maintain full aperture, only decimated datasets where spacing is altered by an integer divisor of 48 were included. Thus datasets decimated by a factor of two, three, four, six, and eight were created (i.e. skipping 5 and 7).

The results of the decimations are shown in figure 3.4. It is clear that the SI technique is capable of reconstructing the main reflection events to a high degree of accuracy even in a poorly sampled regime. This result is encouraging as it indicates that some reflectivity may be retrieved even in non-ideal field scenarios. However, this modelling result may be overly optimistic; the modelling wavelet used here represents a non-realistic field wavelet and the modelling has occurred in a noise free horizontally layered medium.

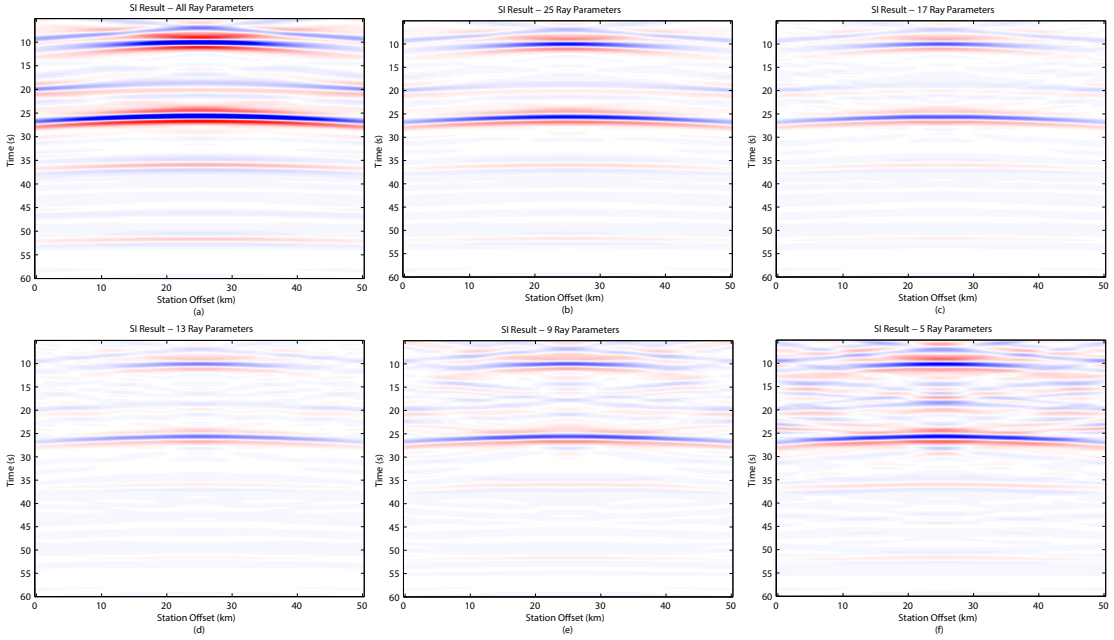

Figure 3.4: The decimation study results are shown; from panel (a) through (f) the total number of unique ray parameters used to create the SI virtual record are reduced.

3.5 Source Time Function

Before proceeding to the 2D modelling, an important investigation into the source mechanism of earthquakes is required. A complicating factor in utilizing earthquake events as an imaging source is the complexity of the source character, oft referred to as the source time function (STF). The design of an STF requires that the physical process of faulting be considered (a discussion of this topic can be found in Stein and Wysession (2009). The frequency and phase spectrum of the STF is influenced by the earthquake rupture and rise time, depth, reverberations from structure

near the source, earth's intrinsic preferential attenuation of high frequency content, and distance from the receiver. These factors need to be modelled in order to create a source signature that can predict complications expected in a field dataset.

The duration of the STF signal is typically taken as the convolution of two box-car functions. One of these box-car functions represents the rise time T_D; this is understood as the duration under which slip along the fault occurs. The second box-car function represents the rupture time T_R, which is the time taken for the fault to rupture at a velocity dictated by the material properties. Furthermore, in the code used to generate the source time function, consideration was given to other physical properties effecting the shape of the function. Source side reflections from the free surface are included; one reflection representing the sS phase, and another higher velocity, lower amplitude, reflection representing pS phase. Additional reduced amplitude reverberations are included to represent wavefield modulation by near surface source side material contrasts. Attenuation is determined by travel time and an average Q factor for mantle materials. Temporal separation of the surface reflections and subsurface reverberations are modulated by an event depth parameter. All of these factors are combined to generate an STF that reasonably simulates the potential complexity of a field recording; figure 3.5 shows two random STFs generated by our method.

Next, our method was used to generate a series of 49 STFs that replace the original wavelet in the original transmission responses. When SI is applied to the STF dataset, the resulting SI virtual record is much less clear and the quality heavily depends on the frequency content in the STFs. The complex character of each STF resulted in some individual amplitude spectra containing significant notches where other STFs contained energy; having a comparable frequency spectrum between individual input sources is a prerequisite for SI success. Spectral whitening is thus applied to each STF transmission response that was used to create the composite in figure 3.6. While this result has a considerably lower resolution than the SI result created with the transient wavelet, strong reflections are still identifiable. Determining ways to reduce the detrimental effect of the complicated STFs on the SI output is of significant importance and is discussed in the following chapter.

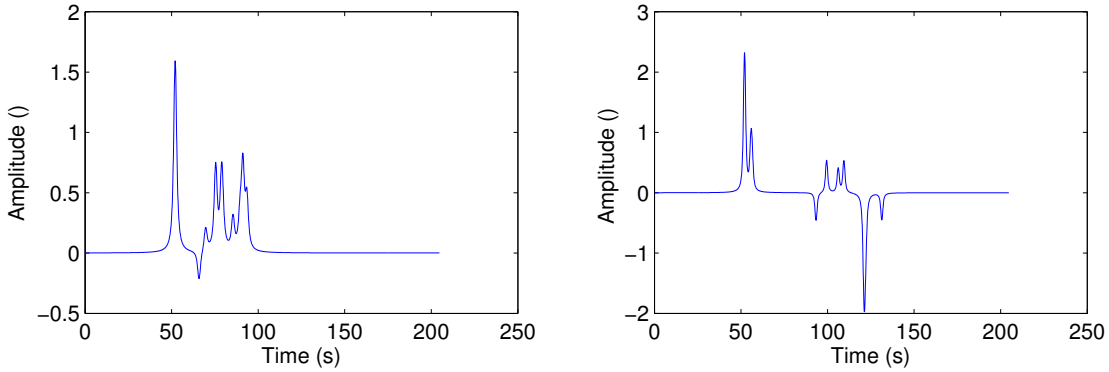

Figure 3.5: Two generated STFs are shown. Note the variability in number of reverberations (small amplitude peaks and troughs) and trailing larger amplitude reverberations from free-surface reflections. The time scale is shown in seconds, demonstrating the period over which energy is distributed.

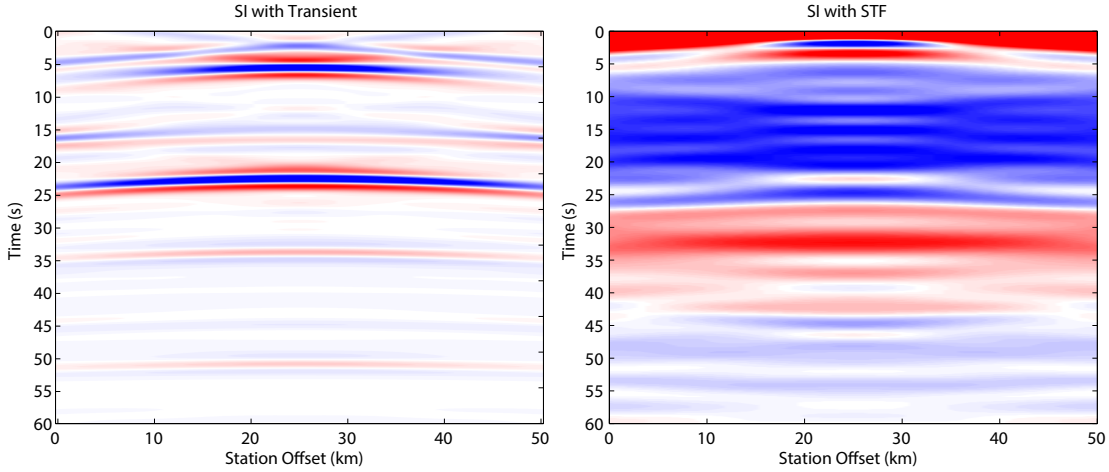

Figure 3.6: Comparison of the virtual source record resolution achieved by SI with the transient modelling wavelet and the STF effective wavelet. Dramatic reduction of frequency content results in significant loss of vertical resolution. Primary reflections are still accurately reconstructed.

Chapter 4

2D Modelling

4.1 The Model

The subduction setting for southern Mexico features a horizontal oceanic slab (the Cocos plate), which begins to dip steeply beneath the thickened crust and mountainous region surrounding Mexico City. Refer to the work by Pérez-Campos et al. (2008) for further reference regarding the interpretation of this region. A 2D model was developed to provide insight into which processing techniques may be used to improve imaging capabilities for field datasets and potential obstacles. Existing literature documents some features of the subduction setting, such as the low velocity zone attached to the top of the subducting slab, the relative location of the slab itself, and tomographic velocity contrasts (Pérez-Campos et al., 2008); however, little information was available regarding absolute velocities. Another source (Contreras-Reyes et al., 2012), provided information with detailed velocity values for a subduction zone with similar geological features to those in southern Mexico; this information was used to define the velocity structure of the 2D model. As the MASE array features 100 seismometers at approximately 5 km intervals, we create a 2D model with 251 seismometer stations distributed over a linear 500 km. This is finer sampling than the real data, but allowed for further experimentation with an increased spatial sampling. Decimation was later performed to reduce the number of receiver locations to 126. Shear wave propagation velocities in the model range from 3030 m/s in the low velocity zone atop the subduction slab to 4677 m/s in the deepest section of the model (Figure 4.1. The novel approach of using an RGB image to create this model is described in Appendix A.

Similar to the 1D modelling, a series of 49 plane waves were propagated through the model at ray parameters from -0.120 s/km to 0.120 s/km at increments of 0.005 s/km to generate the transmission responses. The initial results were created using a first order derivative of a Gaussian function with a maximum and dominant frequency of 1.0 Hz and 0.45 Hz, respectively. Again, the transient wavelet represents an ideal scenario; later, we replace this wavelet with the complex STF. An example of the appearance of a transient recording is seen in figure 4.2. Note that in all figures, positive polarities (a hard kick) are depicted in red. To prevent aliasing in the forward modelling, a sample interval of 0.01 s is used; reduction of this interval is later applied to reduce computation time and file size.

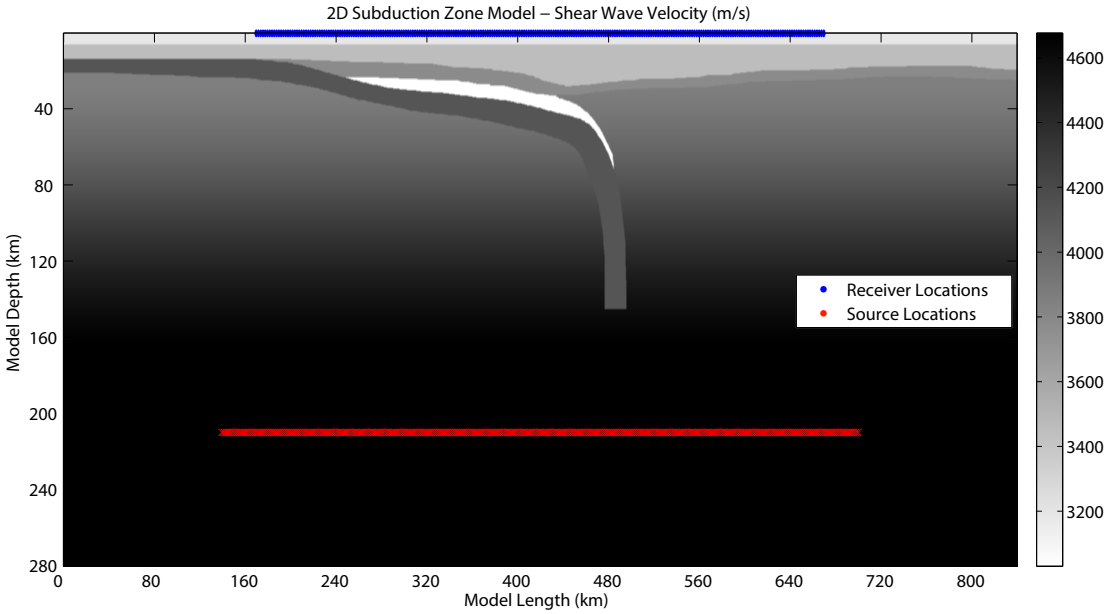

Figure 4.1: 2D shear wave subduction model. Receiver positions are indicated in blue and subsurface source locations are indicated in red. Velocities range between 3030 to 4677 m/s.

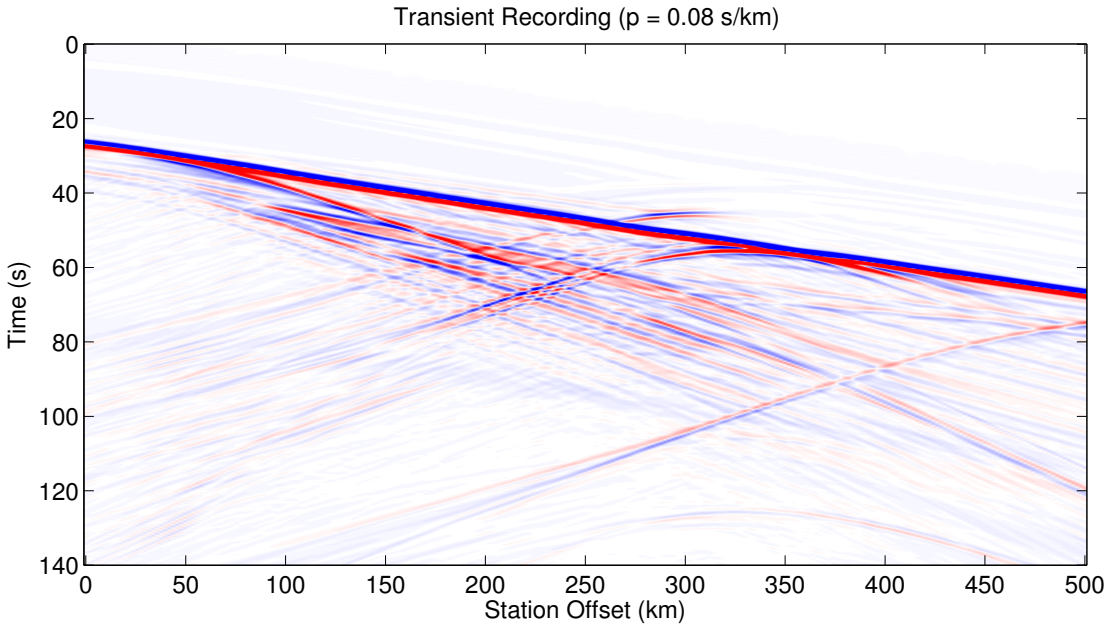

Figure 4.2: A typical transient recording. Here, the ray parameter 0.08 s/km is shown.

4.2 STF Application

The transient wavelet was removed from each record (by deconvolution of the known signal) and a unique STF was convolved with the remaining reflection response. An example of the typical duration and character of a random STF is shown in figure 4.3. The same transmission response in figure 4.2 is now shown with the STF effective wavelet in figure 4.4. Note that the apparent difference in the angle of the direct wave in the STF recording compared to the transient recording is merely due to the difference in duration of the time axis. A detailed view is given in figure 4.5. The STF, which contains energy distributed over significant temporal duration necessitates a longer record length to capture the full transmission response and reflected multiples.

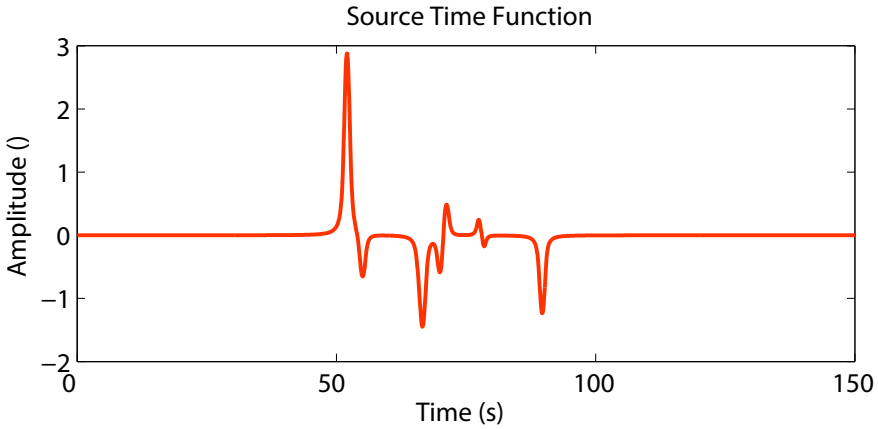

Figure 4.3: A STF used to simulate earthquake source characteristics.

The STF complicates the appearance of the transmission response quite dramatically. It is evident in figure 4.4 that the receiver-side reverberations are still present in the data, but the resolution of the response is reduced considerably from the transient wavelet case. This loss of resolution occurs primarily due to two reasons. First, the distribution of wavelet energy in the STF occurs over a long duration; the time between the direct arrival and final source side reverberations may span several tens of seconds. Second, the average frequency spectrum of a given STF heavily favours the extremely low frequencies, with the peak typically near 0.1 Hz and a maximum frequency near 0.5 Hz. Techniques to mitigate the lost vertical resolution is a significant focus of this chapter.

4.3 Transmission Response Improvement

The long temporal energy distribution and relatively low frequency content within the STF is undesirable for imaging purposes; therefore, techniques that can reduce the duration of the effective wavelet, or mitigate its effect, should be applied. In order to achieve this, various techniques including decomposition, deconvolution, and whitening, are tested. Decomposition refers to the separation of the incident P and S fields, similar to the situation described in chapter 3. Deconvolution attempts to compress the effective wavelet to increase the temporal resolution of the data. Before directly testing deconvolution, techniques to estimate the character of the

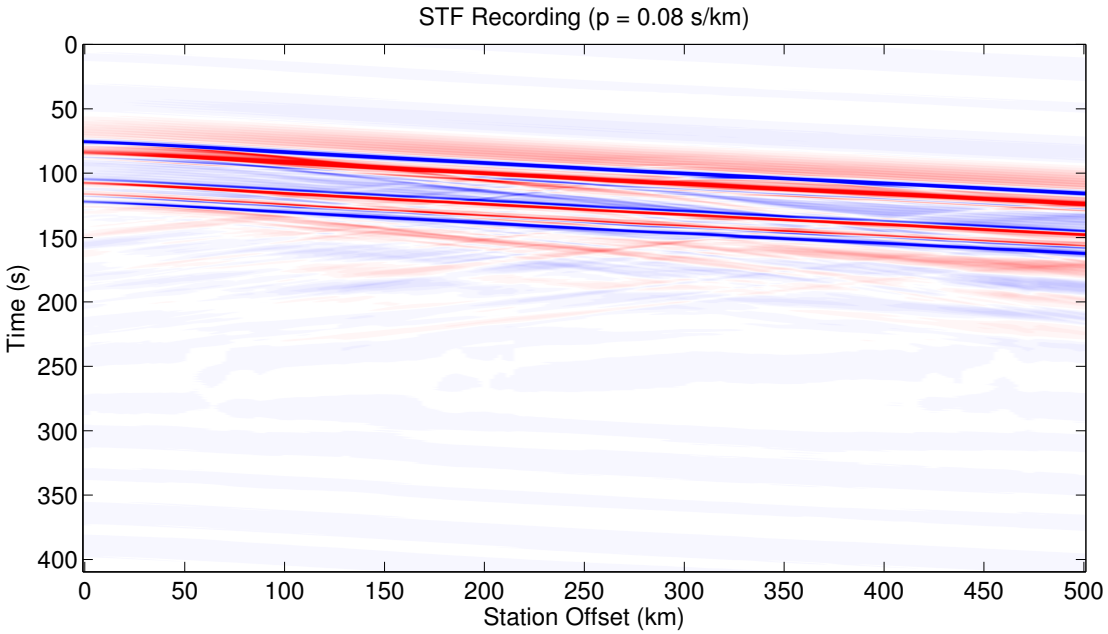

Figure 4.4: A transmission response with the STF replacing the transient wavelet.

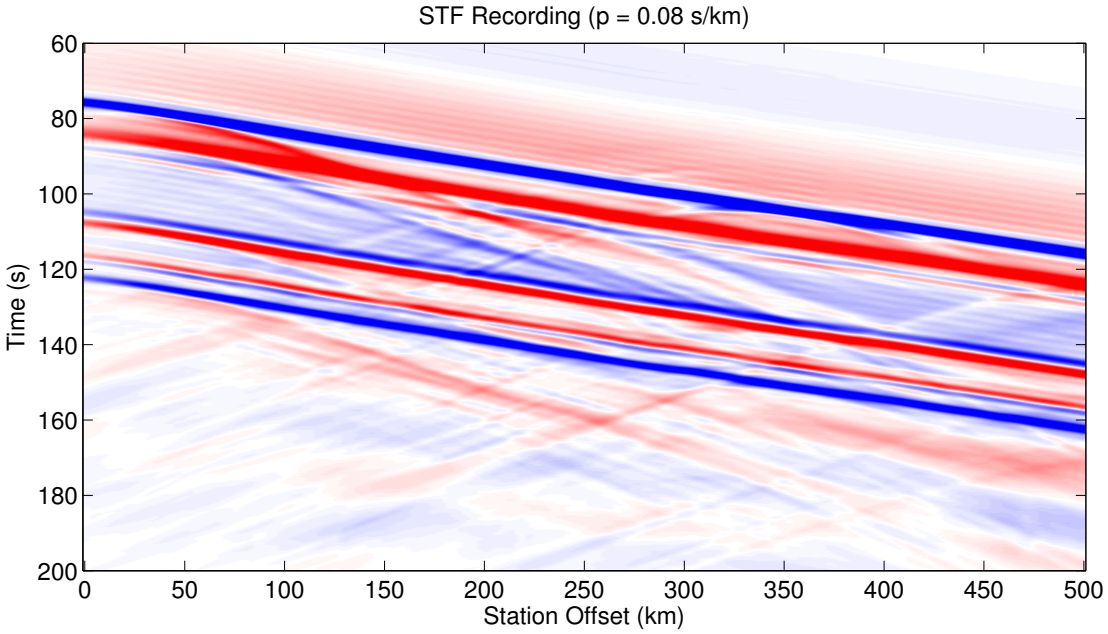

Figure 4.5: A transmission response with the STF replacing the transient wavelet; detailed view.

STF are applied. Two forms of deconvolution are tested; namely, Wiener deconvolution and spectral division. Lastly, spectral whitening (herein referred to simply as whitening), compares the amplitude of individual frequencies present in the spectrum of a given response and normalizes the frequency content over that bandwidth.

4.3.1 Decomposition

It is useful to revisit the topic of decomposition for the 2D case. In the 1D situation (Section 3.2) it was difficult to determine the utility of decomposition due to the horizontal structure and limited mode converted energy present. In the 2D case, it is much clearer what benefit can be achieved, both in the transmission responses as well as the SI result. To clearly illustrate the effect of decomposition, we focus on transient wavelet transmission response images. Whatever benefit achieved in the transient wavelet case will be achieved in the STF case; this is because decomposition is independent of data complexity, it depends solely on propagation velocities and the ray parameter of the response.

In figure 4.6 the radial component of the transient recording is shown prior to decomposition. Compared to figure 4.7, which shows the decomposed recording, it is clear that some arrivals are severely suppressed. The energy arriving prior to the S wave direct arrival (the high amplitude arrival at approximately 80 s near the 0 km mark) is mode converted SP energy. Comparing the two images, it is clear that the decomposition technique removes the majority of this energy from the transmission response. Although the application of SI will be discussed later, we present the effect of decomposition in an SI record here for the sake of clarity. The impact of decomposition on the SI results can be seen when comparing figure 4.8 and figure 4.9. The region between the direct arrival and reflectivity is obscured by SP converted energy in figure 4.8. The energy in this area is considerably reduced by the decomposition process as seen in figure 4.9. Decomposition is evidently beneficial for improving the clarity of the transmission responses and SI results. Therefore, this processing step is applied to all transmission responses in the dataset. Note, however, that a certain form of mode converted cannot be removed. Although the S phase dominates the energy recorded, there is still an element of SPS converted energy. The decomposition technique is capable of removing the converted P energy, but reconverted S energy is indistinguishable from S energy.

4.3.2 STF Estimation

In order to apply deconvolution, it is first required that an estimate of the STF be available for filter design. Since the STF is propagated with a fixed ray parameter across the entire recording, it is possible to estimate the STF character by extracting the characteristics of the recording that remain constant from trace to trace. In practise, this is achieved by "flattening" the recording via an estimate of the ray parameter judged by the difference in arrival time of the direct arrival between the receiver points. With the transmission response flattened, fine adjustment of the traces can be achieved via static corrections. The sum of all traces of this flattened recording provides the STF estimate. Note that some of the reflectivity might map into the STF estimate, especially when receiver-side structure does not show much variation from station to station. This process is demonstrated in figure 4.10, with the resulting estimate shown in figure 4.11. The estimate is a close match to the actual waveform, but significant side lobe energy is present. It is difficult to remove this side lobe energy in any deterministic manner as it varies between

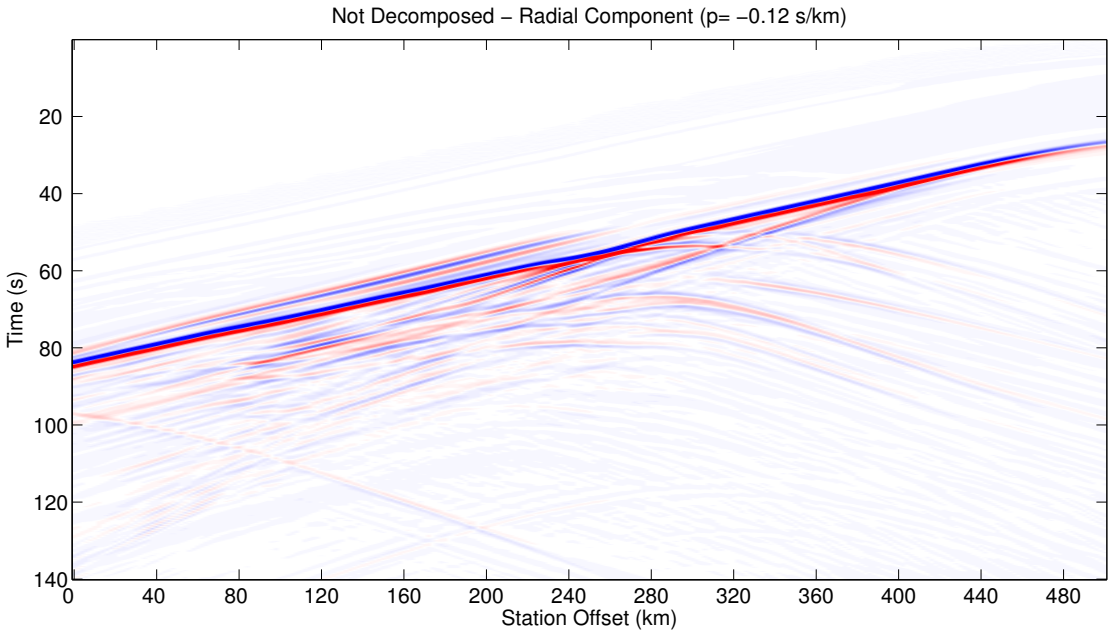

Figure 4.6: Transient wavelet transmission response before decomposition. The ray parameter is -0.120 s/km in this transmission response.

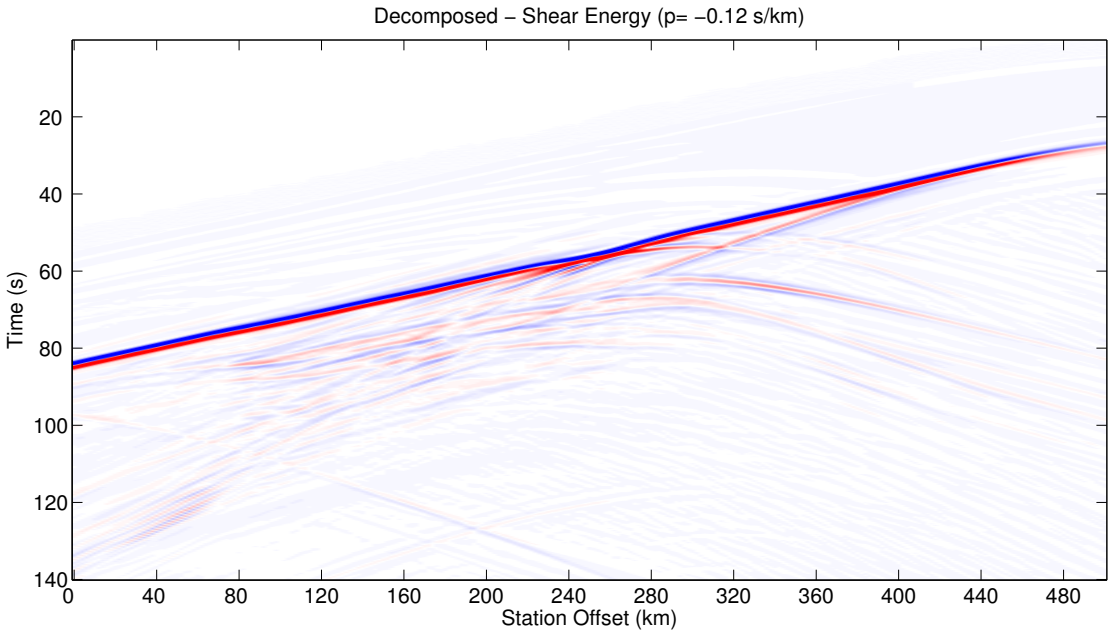

Figure 4.7: Transient wavelet transmission response after decomposition. The ray parameter is -0.120 s/km in this transmission response.

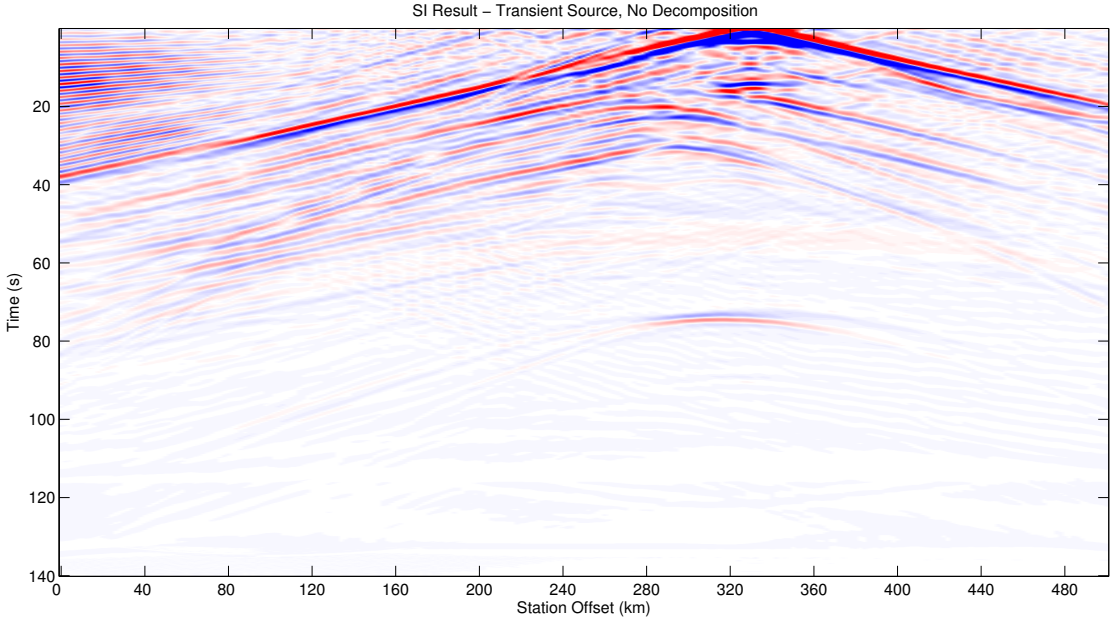

Figure 4.8: The SI virtual source record with a receiver located at 328 km used as the virtual source. This response is created from a dataset without decomposition applied to the transmissions.

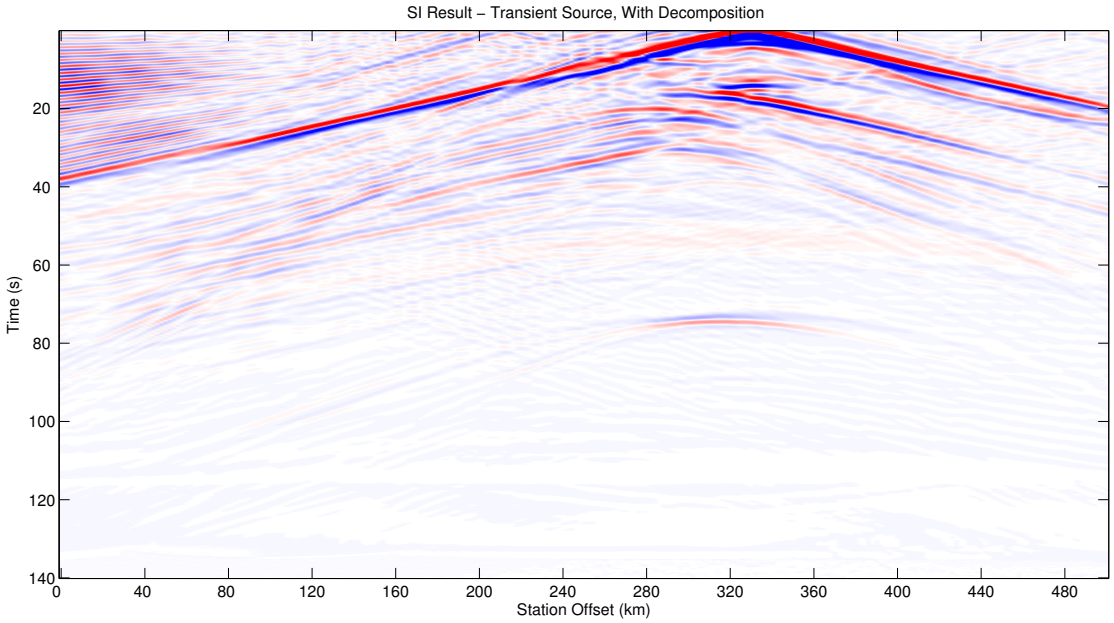

Figure 4.9: The SI result with a receiver located at 328 km used as the virtual source. This response is generated from the same dataset as the figure 4.8, but with decomposition applied to the transmission responses.

STF estimates, with the amplitude spectra of the side lobes overlapping with the STF. The impact of this effect will be discussed below in the deconvolution section.

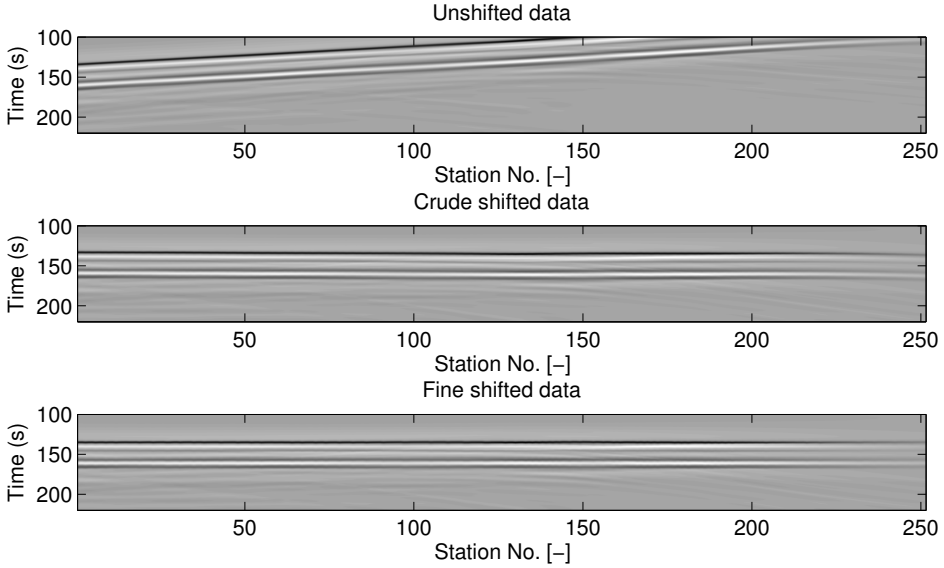

Figure 4.10: Demonstration of the STF estimation process. The top panel shows the transmission response without any shift applied. The middle panel shows the shifted response based on a ray parameter estimate from the arrival time of the direct arrival. The final panel shows a fine adjustment based on a statics comparison applied to neighbouring traces.

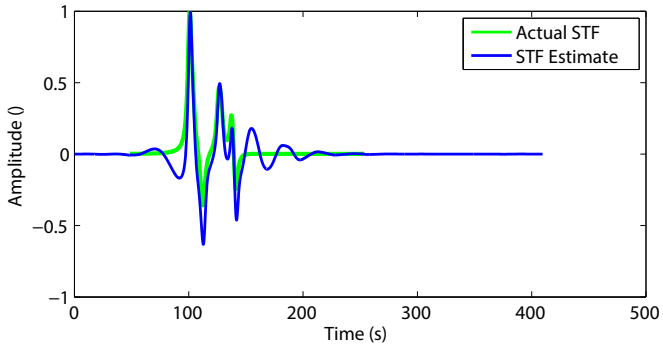

Figure 4.11: Result of STF estimation technique; note the presence of side lobe energy in the estimate. This energy is a primary reason for difficulty in deconvolution application.

4.3.3 Deconvolution

All deconvolution algorithms make use of the convolutional model for seismograms. A recorded signal is assumed to be the product of convolving a seismic wavelet and a reflectivity profile, where noise is included as an additive term. Deconvolution attempts to improve vertical seismic resolution by shaping the effective wavelet into a spike or compressed wavelet at zero or arbitrary lag. Removing the wavelet should leave a reflectivity profile where elastic impedance contrasts are represented by positive or negative spikes. Two methods of deconvolution are tested for appli-

cation; spectral division and Wiener deconvolution. Spectral division is applied in the frequency domain and Wiener deconvolution is implemented in the time domain. In order for deconvolution to be applied successfully, there are a set of assumptions that are normally considered (Yilmaz, 2001); the primary assumptions pertinent to our situation are the assumptions that the source wavelet is known, and more importantly, that it is minimum phase. A minimum phase signal necessitates a stable minimum phase inverse; this is not the case for a mixed phase signal, such as our STF.

It should be noted that for the further processing described in this chapter the dataset has been decimated from the original state. The original modelling contained 251 receiver positions, but is now reduced to 126 positions. The original forward model was sampled at 0.01 s to insure against aliasing, the following steps use a dataset decimated to 0.1 s to significantly decrease computation times (without loss of accuracy).

Spectral Division

Spectral division, as the name implies, is a deconvolution technique that attempts to improve the resolution of the recordings by dividing the frequency and phase spectrum of the recording by the spectrum of the effective wavelet. By dividing each frequency present in the recording by the content of the effective wavelet, the frequency content is normalized across the spectrum. Unlike whitening, spectral division is also applied to the phase component of the trace, ensuring consistency in phase. In order to preserve stability of this operation, a small level of prewhitening is added to the filter design. This prevents amplifying frequencies not present in the recording by essentially dividing by zero. As the process is designed to remove the effect of the recorded STF, the filter design used should be the best estimate of the STF available. As illustrated in figure 4.1, the STF estimate available is a close match to the true STF, but features some undesirable side lobe energy. As discussed above in section 4.3.2, there is no way to deterministically isolate the true STF estimate from the undesirable side lobe energy. The implication of this is that the final result typically features some ringing and loss of resolution despite the method's ability to tighten up some of the STF character. When testing this method with the true STF, a near perfect result is attainable; however, in field scenarios, the luxury of precisely knowing the effective wavelet is, of course, unavailable. Given these results, deconvolution by spectral division is not recommended as a preprocessing step for SI.

Wiener Deconvolution

Wiener deconvolution attempts to remove the effective wavelet present in the dataset by minimizing the least squares error between a desired output (in our case, a zero-lag spike) and the autocorrelation of some input signal (Yilmaz, 2001). The result of this process creates a shaping filter that converts the input signal into a zero-lag spike. This shaping filter is then convolved with each trace in the dataset, and is optimal in the sense that it minimizes the error between the input signal and desired output, effectively removing the source signature.

Applying deconvolution to a dataset typically takes much experimentation to find the best value for a series of parameters; there is no best solution available by default. Wiener deconvolution requires testing for the optimal input signal and length of the inverse filter (i.e. the number of autocorrelation lags permissible in the filter design). There are essentially two choices for the input signal; the STF estimate generated as described previously (Section 4.3.2) or the trace itself. Assuming the reflectivity of the subsurface is white, the trace should provide a good estimate

of the STF; in practise, a given reflectivity profile is not white and may introduce errors. In our testing, the result obtained when using either the STF estimate or the trace itself as the filter design yielded little difference. The filter length, however, played a more significant role. The optimal number of autocorrelation lags is found to be near 100 samples (10 s) in duration. Including more lags had mixed results; while sharpening some features, it also introduced an undesirable ringing character that impaired the overall clarity.

We illustrate the deconvolved transmission response of the record in figure 4.4; the best result achieved with the Wiener deconvolution technique is shown here in figure 4.12. Note that applying the filter converts the dataset to zero phase; this is due to the fact that the autocorrelation of input signal is used to create the optimal shaping filter. The vertical resolution is certainly improved by this technique, but note how there appears to be an introduction of ringing despite limiting the length of the autocorrelation lags. This is due to the fact that either filter design (whether the STF estimate or trace itself is used) is not minimum phase. The instability of its inverse leads to a solution that inevitably includes some degree of ringing. While in a normal processing flow this small level of ringiness may be acceptable given the improvement in resolution, this may introduce an undesirable effect in the SI result.

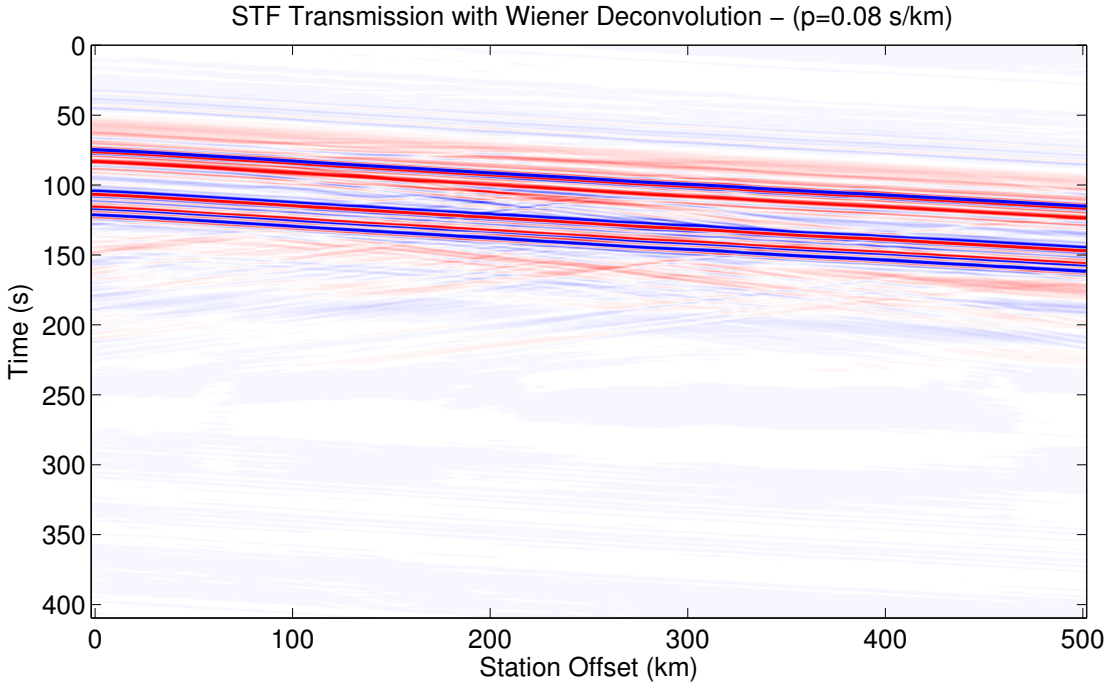

Figure 4.12: An example of an STF recording with Wiener deconvolution. There is a definite improvement in vertical resolution, but an increased presence of ringiness (compare to figure 4.2 and 4.4). This ringiness leads to spurious cross terms in the SI result.

4.3.4 Whitening

Whitening is a technique that normalizes the amplitudes of a given signal's frequency spectrum. Unlike spectral division, which depends on the frequency and phase content of the effective

wavelet to improve resolution, whitening simply normalizes the spectrum of the recording for each trace as a whole. SI assumes that the autocorrelation of the STFs is equal from source to source (Wapenaar and Fokkema, 2006). In practise, the sources occurring in any field always vary from record to record. Even if the source is controlled to a high degree of accuracy (i.e. in the case of vibrator sources), variation in surface coupling or the near subsurface removes any expectation of a perfectly repeatable source. While a white spectrum is unachievable in the field, SI remains possible if the spectrum of individual sources contain the same frequencies after whitening.

Whitening is implemented by normalizing frequencies in the amplitude spectrum. The average power is computed within a window of the frequency spectrum; the central frequency within this window is then normalized and the window is moved along the spectrum by one sample. This process is repeated over the full spectrum. A bandpass filter is applied to the whitened section to prevent amplification of frequencies not present in the recording. Figure 4.13 is included for comparison to figure 4.4. In figure 4.13, no processing other than whitening is applied, yet considerable improvement is clear. A detailed view is given in figure 4.14. The record is still dominated by the effect of the STF, but the visibility of reflectivity in the background is encouraging.

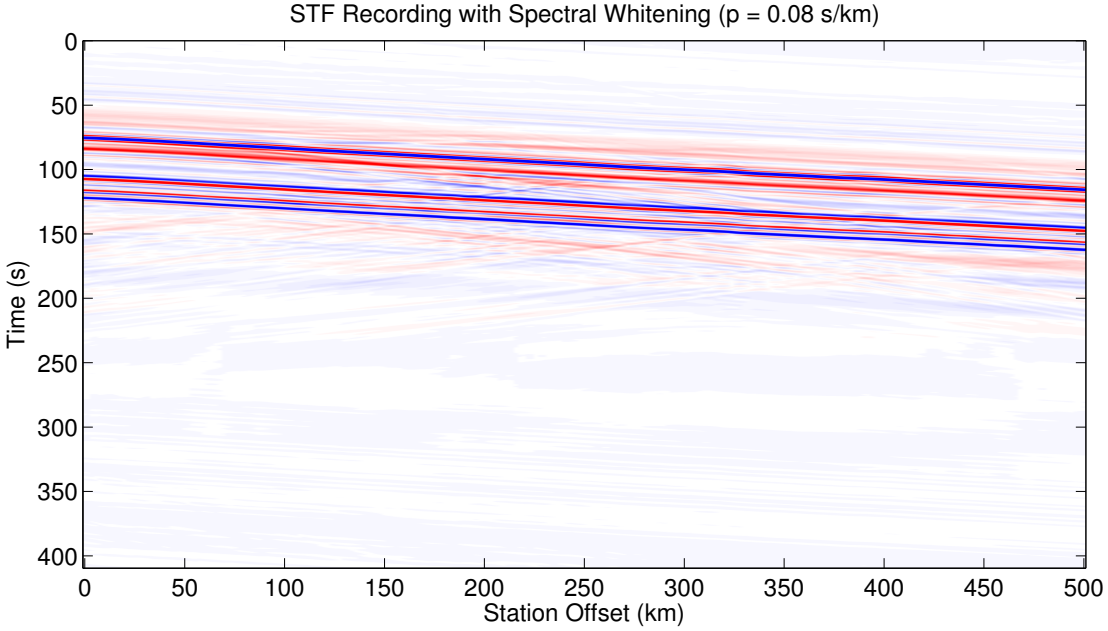

Figure 4.13: An example of an STF recording with only whitening applied. Note the presence of reflectivity at approximately 300 km offset. Although obscured by the reverberations of the STF, the reflectivity is still visible and later retrievable.

4.3.5 STF Removal Discussion

The results obtained by implementing deconvolution are unsatisfactory. Although two processing techniques were applied in an attempt to improve the shape of the effective wavelet, the complex and temporally distributed nature of the STF defies useful application of deconvolution. Modern

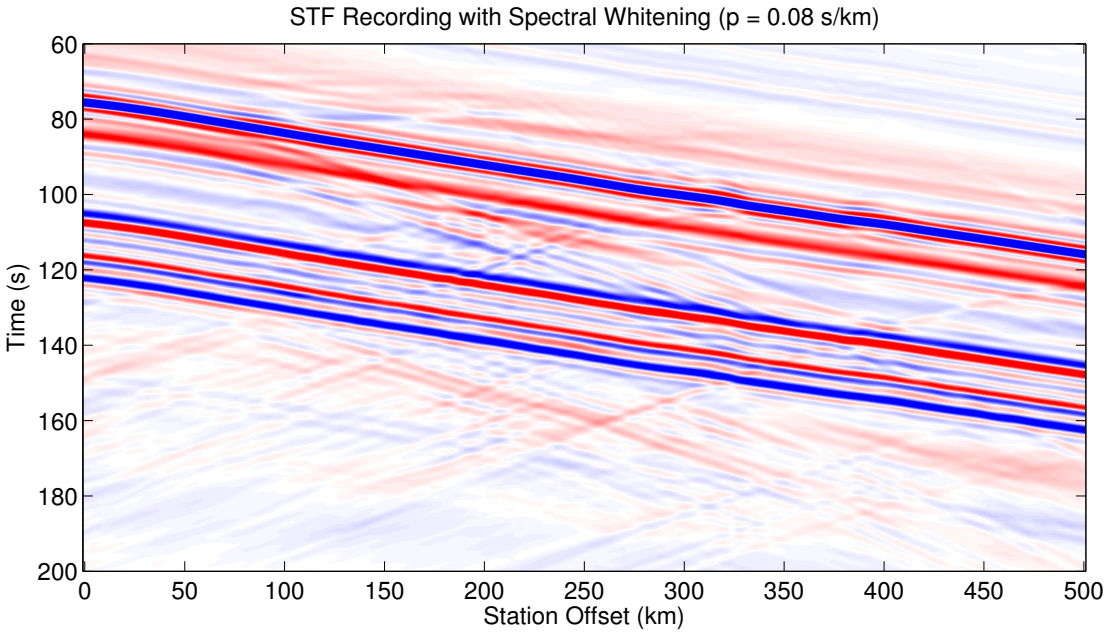

Figure 4.14: A detailed view of the data in figure 4.13.

research is focusing on this issue directly; an attempts to normalize the effective wavelet prior to further processing is seen in the work of Bostock (2004). This line of research is important for earthquake seismology; with the complication of the STF being unavoidable, mitigation techniques are necessary. At this point, whitening remains as a technique that improves the appearance of the transmission recordings. Reflectivity is more clearly visible after whitening among the low frequency reverberation that previously dominated the recording (Figure 4.13). Furthermore, whitening is necessitated by the theory of SI and is applied to all transmission responses.

4.4 SI and Correlation Panel Filtering

We proceed with the STF transmission responses with whitening applied. Up until this point, the attempted improvements have taken place prior to commencing the SI operation. While it remains possible to improve image quality with conventional pre-stack and post-stack techniques, SI improvements could also be achieved by isolating features that reach stationarity in the correlation panel. The correlation panel, as defined here, is produced in the argument of the integral in equation 2.2. The integral represents (in a discrete source distribution scenario) the summed effect of the crosscorrelation of a receiver at position $\mathbf{x}_B$ with position $\mathbf{x}_A$. This crosscorrelation of a fixed source position with a fixed receiver position creates a new "trace" within the correlation panel for each transmission available. In the discrete case presented here (49 transmissions), these "traces" can be stored separately prior to summation. At this stage, it is possible to apply further processing to isolate reflectivity from physical features and eliminate spurious cross terms.

In theory, the events that offer a physical contribution should reach stationarity in the correlation panel (Snieder, 2004). Although the plane-wave sources (complicated by the STF) travel at different ray parameters through the surface, the travel time difference, in the correlation panel, between virtual source position and a receiver should reach a stationarity near one of the source positions. In practise, since the source bandwidth is not a spike, stationarity is present over multiple traces. This stationarity is often not present with the spurious cross terms generated by the STF or, in theory, random noise. With this understanding, it is possible to test different filtering techniques in the correlation panel that preserve the stationary phase components and discard the rest. Two improvement techniques were investigated here; singular value decomposition (SVD) and wavenumber (k) filtering.

4.4.1 Singular Value Decomposition

SVD operates by decomposing a given m x n data matrix (D) into a three separate matrices according to

$$D = U\Sigma V^t, \tag{4.1}$$

where U is n x n, V is m x m, and Σ is m x n. Σ is zero everywhere except for the main diagonal, which contains positive, real valued, entries. These values descend in magnitude from the first entry to the last, with the larger values corresponding to low wavenumbers (Melo and Malcolm, 2011). For a more detailed discussion of the theory regarding the relationship between wavenumber (called frequency in some sources) and SVD, refer to Hansen et al. (2006). As discussed above (Section 4.4), physical events should reach stationarity in the correlation panel, therefore removing small valued singular values from Σ and reconstructing D should suppress spurious cross terms created in the crosscorrelation step. Taking the transpose of the correlation panel is necessary because the stationarity occurs in the spatial dimension; the transpose allows the SVD algorithm to run efficiently in the vertical dimension as shown in Melo and Malcolm (2011).

A degree of arbitration is required to determine the number of singular values to retain. Unlike a textbook example where a strong drop off from desirable singular values to noise-correlated singular values exists, our situation is ambiguous (Figure 4.15). The left panel demonstrates the normalized singular values retrieved from a correlation panel in our dataset. It is difficult to determine which singular values to discard as the singular values decrease monotonically across the matrix. The right panel shows a synthetic example where determining the singular value cut off is clear. In order to determine an appropriate level of singular value reduction, several trials were performed. By using receiver position 83 (a position selected near the hinge of the subducting slab, see figure 4.1) as a virtual source to position 80, the correlation panel in figure 4.16 was generated. The spatial separation between the receiver positions is only 12 km, hence the zero lag position has hardly any noticeable move out over the source positions. SVD appears to effectively remove the spurious cross terms, and looking closely at the final panel, it is possible to see the locations of stationary phase.

Another example is generated using position 83 as a virtual source to receiver position 20. The same format as figure 4.16 is used in figure 4.17. The greater offset (252 km) between these locations results in the increased move out of the zero lag position between traces. This figure reveals a problem encountered when applying SVD to long offset cases. Note the apparent improvement in the top panel; a clear reduction in some of the high frequencies (spurious cross

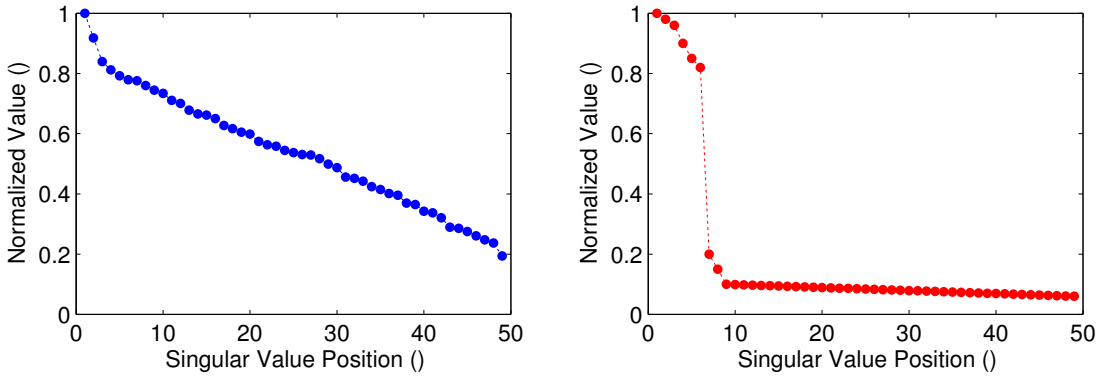

Figure 4.15: The left panel shows the singular values retrieved from the correlation panel with virtual source position 83 and receiver position 80. The right panel shows a theoretical case where the difference between singular values to retain and those to discard is clear.

terms) is apparent. From the theory described in Melo and Malcolm (2011), this is desirable. However, by the time the final panel is reached, there seems to be exaggeration of some non-physical feature, notably the thick banded reverberation in the horizontal dimension. This is the low frequency reverberation present in the model noted previously. Essentially, there is little energy that remains in the stationary phase, thus the only feature to survive SVD is the low frequency artifact.

Selecting the optimal number of singular values to preserve or discard remains ambiguous. Therefore, an investigation into the SI result with SVD preprocessing is required before any conclusions can be drawn. While the correlation panels demonstrate the effect for a single pairing of a virtual source location and a fixed receiver, looking at a full virtual source record is illustrative. Using receiver position 83 as the virtual source (328 km offset), figure 4.18 shows the end SI product produced using a "mild" level of singular value removal (19 values retained). Figure 4.19 shows the result obtained preserving only 5 singular values. Finally, figure 4.20 shows the result when only 3 singular values remain. The general effect is that long offset energy is reduced proportional to reduction of singular values. Compared to the situation where no SVD is applied (Figure 4.21), this does not appear advantageous. Looking specifically at the spurious direct arrival, the SVD process does significantly attenuate the spurious arrival as it has large move out in the correlation panel at long offsets. However, at near offsets, in the correlation panel, the move out is smaller and the spurious direct arrival is less suppressed. At small offsets, the effect of SVD is negligible in terms of removing spurious cross terms. However, at large offsets, SVD is unable to discriminate reflectivity from spurious cross terms and greatly suppresses both.

4.4.2 Wavenumber Filtering

A wavenumber filter is an obvious choice for preserving zones of stationary phase while discarding undesirable content. Therefore, applying a wavenumber filter that preserves only a small window around k=0 in the correlation panel should enhance reflectivity and suppress spurious cross terms. The effect of this process is illustrated; figure 4.22 shows the correlation panel with no filtering and figure 4.23 shows the effect of a wavenumber filter. The filtered correlation panel appears to be improved; high frequency content appears reduced and lower frequency trends between

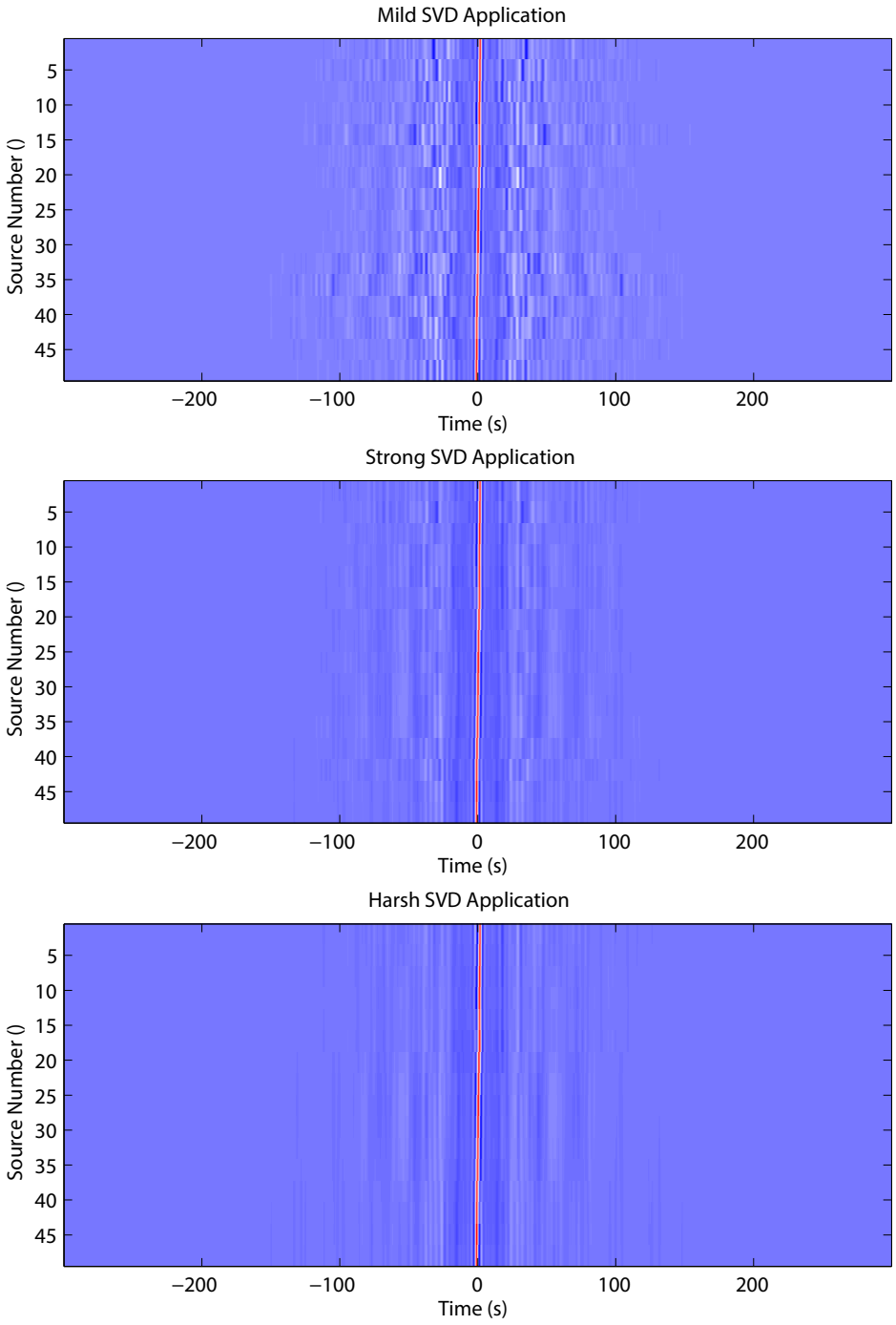

Figure 4.16: An example demonstrating SVD application in the correlation panel. Receiver position 83 is cross-correlated with position 80 for this example. The three panels show varying degrees of singular value reduction; the top panel retains 19 singular values, the middle panel retains 5 singular values, and the bottom panel retains 3 singular values. The stationary events are clear in the final panel with most spurious cross terms removed.

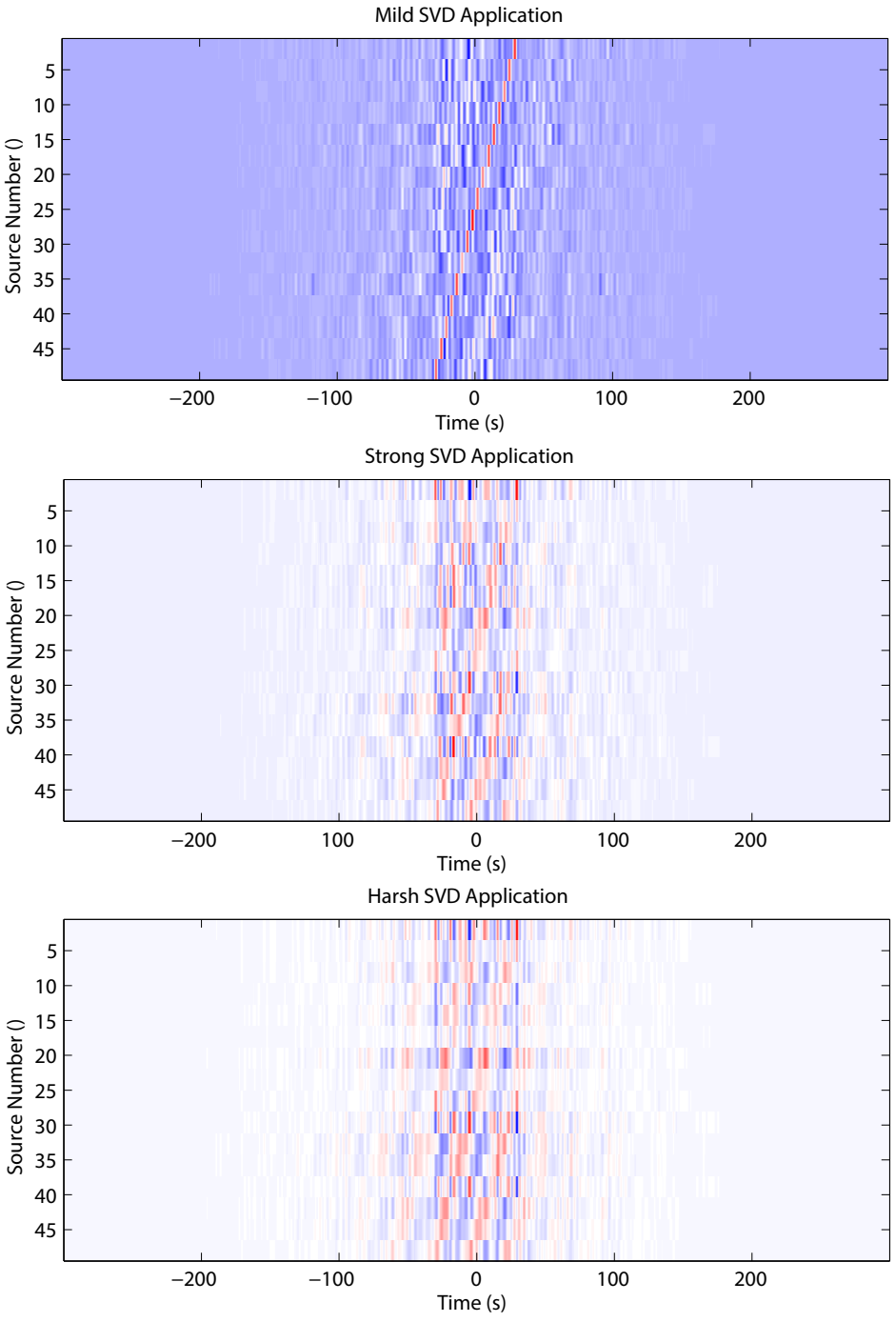

Figure 4.17: An example demonstrating SVD application in the correlation panel. Receiver position 83 is cross-correlated with position 20 for this example. The three panels show varying degrees of singular value reduction; the top panel retains 19 singular values, the middle panel retains 5 singular values, and the bottom panel retains 3 singular values. The majority of the energy present in the panel is removed by the final panel.

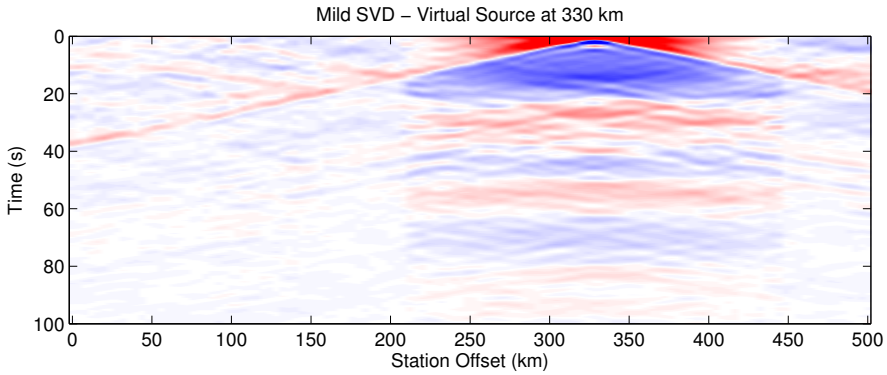

Figure 4.18: The SI output when SVD is applied to each correlation panel used to construct the virtual response. 19 of the singular values are retained.

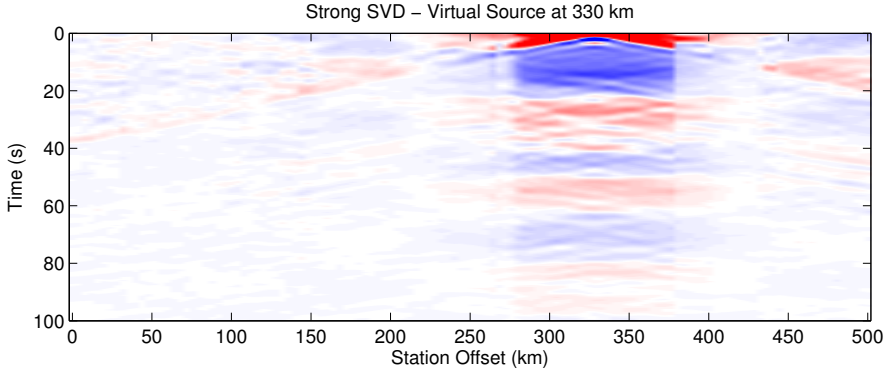

Figure 4.19: The SI output when SVD is applied to each correlation panel used to construct the virtual response. 5 of the singular values are retained.

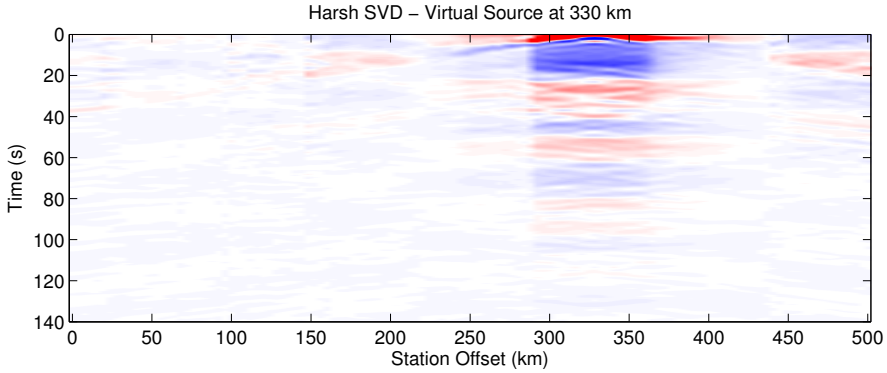

Figure 4.20: The SI output when SVD is applied to each correlation panel used to construct the virtual response. 3 of the singular values are retained.

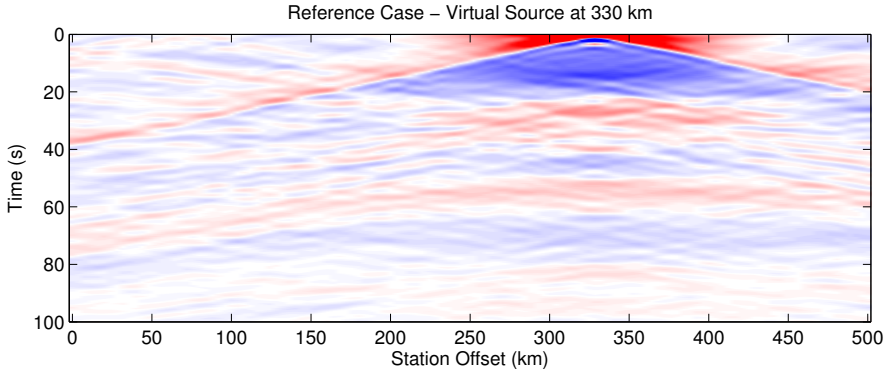

Figure 4.21: The SI output when no SVD is applied.

traces are highlighted. While the correlation panel result looks encouraging, an interesting (and repeatable) phenomenon is exhibited; even though the correlation panel appears clearer to some extent, the effect post-SI is minimal. Figure 4.24 shows the SI result with a virtual source at 328 km without wavenumber filtering. Figure 4.25 shows the same virtual source record with wavenumber filtering applied to each individual correlation panel used to generate the SI record. It is difficult to highlight major difference, but subtle amplitude effects are present.

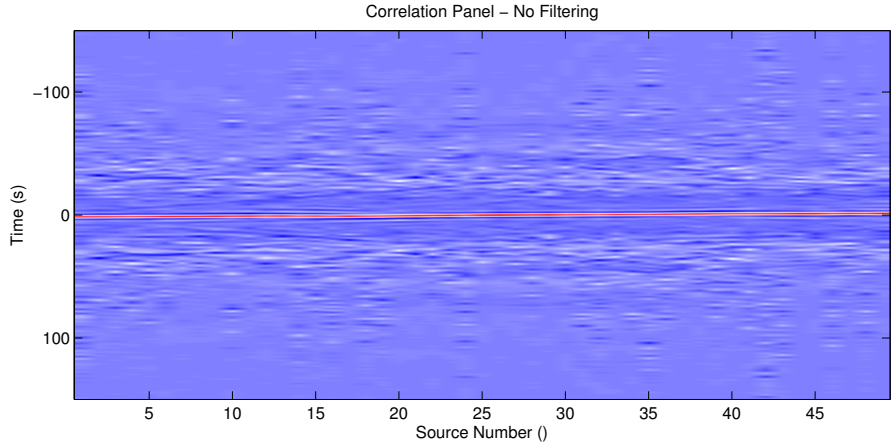

Figure 4.22: A raw correlation panel for virtual source position 83 (328 km) and receiver 80.

4.5 Common Offset Gathers

Sorting data into a common offset gather (COG) acts as another method to check the data quality of the SI results. By sorting traces as a function of offset from virtual source positions, each trace is plotted adjacent to another trace with horizontal subsurface features occurring at similar travel time. We use the term offset to refer to the half distance between source and receiver; convention dictates that the magnitude of offset is the distance to the theoretical midpoint between the source and receiver positions. The zero-offset response gives a good estimation of

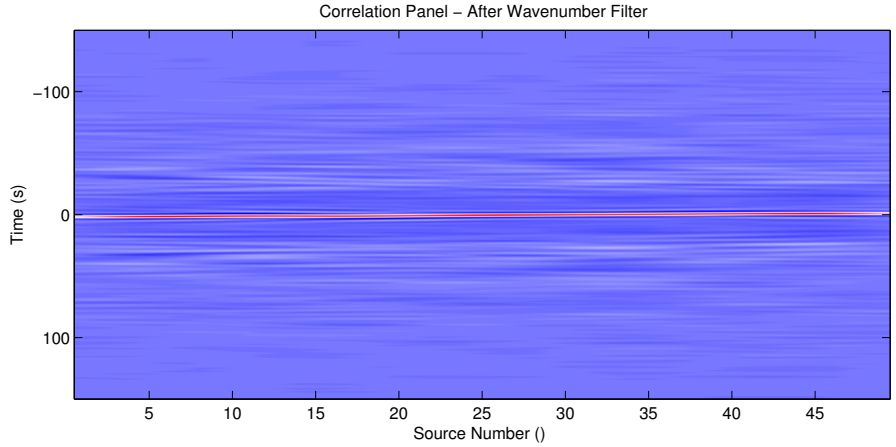

Figure 4.23: The same correlation panel shown in figure 4.22 after wavenumber filtering.

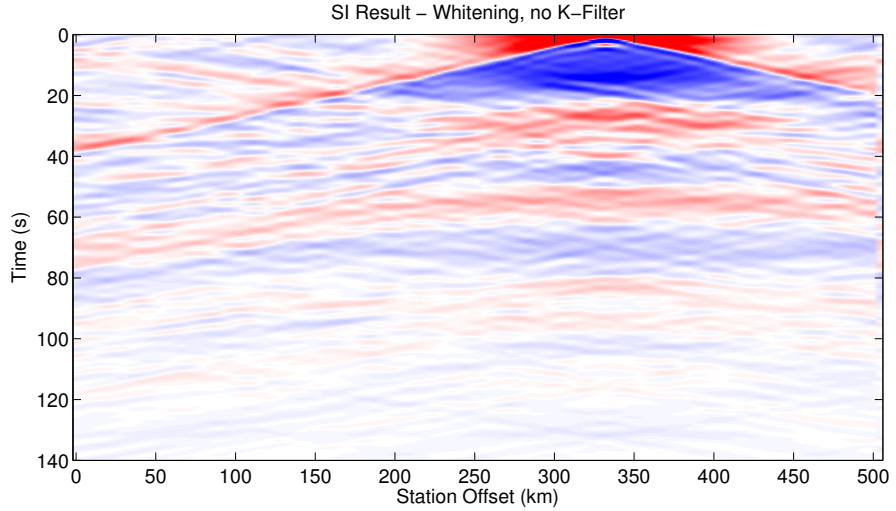

Figure 4.24: SI result for a virtual source at surface position 83 (328 km) with only whitening applied to the transmission responses.

structure. As offset increases, fewer traces are available for comparison in each COG. This is a simple function of the array geometry; midpoint positions located near the centre of the array are typically higher fold (sampled more frequently) than traces near the ends of the profile.

Two further processing steps are applied prior to imaging. The first processing step is to remove the mean horizontal value of each SI virtual source record, thereby removing the low frequency reverberation that dominates the records. This low frequency reverberation is an artifact of the STF crosscorrelation that amplifies energy at a low frequency. This is achieved by first sorting the data into COGs where the artifact appears relatively consistent from trace to trace and subtracting the average value of each row. Comparing the pre-removal figure 4.26 with the post-mean removal figure 4.27 shows the effectiveness of this simple method. Despite this simplicity, a more sophisticated least-squares removal technique does not achieve better results. The second

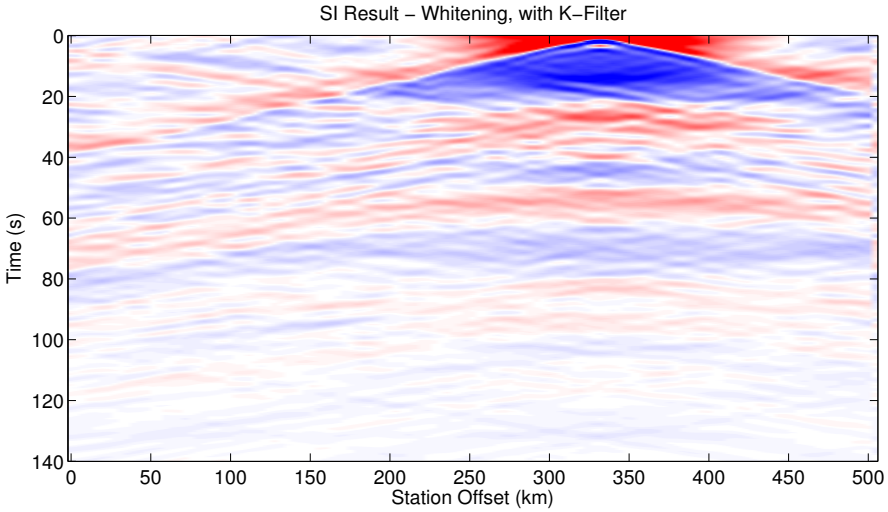

Figure 4.25: SI result for a virtual source at surface position 83 (328 km) with whitening applied to the transmission responses and wavenumber filtering applied in the correlation panel. Nearly zero difference is distinguishable from figure 4.24. Small variations are present in near-zero times, mostly in the non-physical region before the spurious direct arrival.

pre-imaging step is applying a top mute to remove energy prior to, and including, the spurious direct arrival. The spurious direct arrival results from the crosscorrelation of the energy arriving directly at the receiver positions involved in the SI operation. This event is non-physical, and energy arriving prior to this feature is not related to reflectivity. Removal is implemented by determining the velocity of the spurious direct arrival and removing features arriving before that linear feature. This effect can be seen in the upcoming COG-sorted datasets in figures 4.28 to 4.31.

4.5.1 COG Analysis

To illustrate the cumulative effects of the previous processing on the COGs, we generate a series of plots for three of the aforementioned techniques; we use the transient wavelet as a reference case for comparison to Wiener deconvolution, SVD, and wavenumber filtered data. We neglect to plot the whitening only case as it is nearly identical to the wavenumber filter result. Different offsets are plotted for comparison; 60 km offset (COG 66) in figure 4.28, 30 km offset (COG 96) in figure 4.29, 10 km offset (COG 116) in figure 4.30, and zero offset (COG 126) in figure 4.31. A fundamental observation is clear immediately; longer offset examples (especially at 60 km offset) show a drastic decrease in data quality amongst all techniques. At 60 km offset, it is difficult to identify reflectivity in any of the cases, even the transient wavelet appears poorly resolved. By 30 km offset, there is clear presence of interpretable reflectivity. Further, this experiment may offer insights into what offsets are expected to contribute constructively to the following imaging section.

In the previous section, SVD or wavenumber filtering prior to SI did not improve the results with respect to whitening only. While the merit of SVD has been demonstrated in related scenarios (Melo and Malcolm, 2011), based on the data generated here, we recommend not applying SVD as a processing step. Also, the extra computation time required to generate the wavenumber

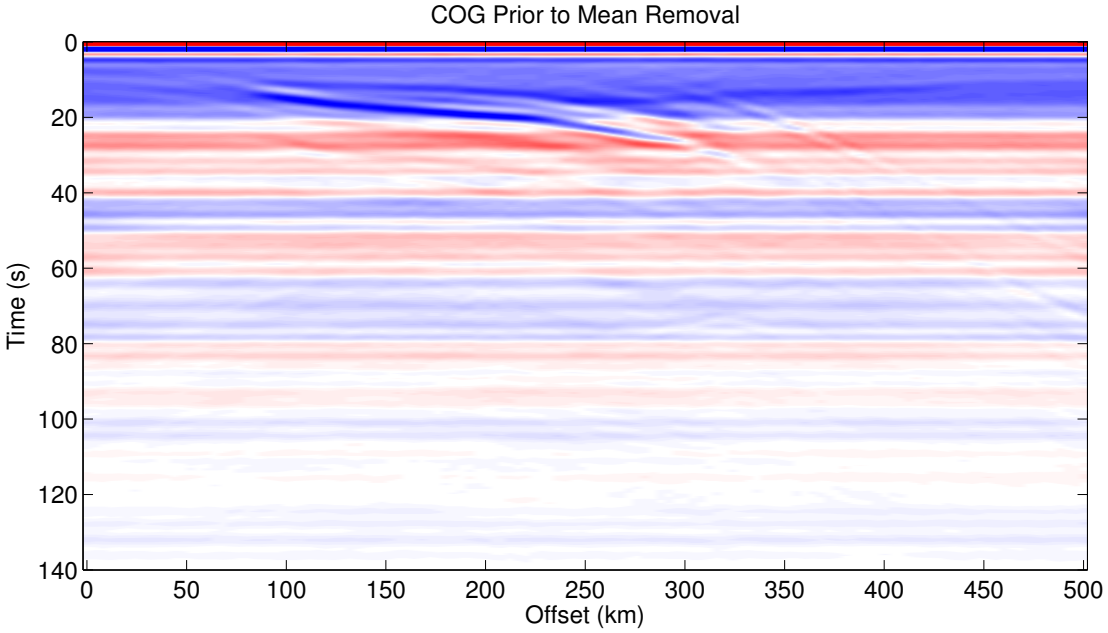

Figure 4.26: A COG example prior to mean removal.

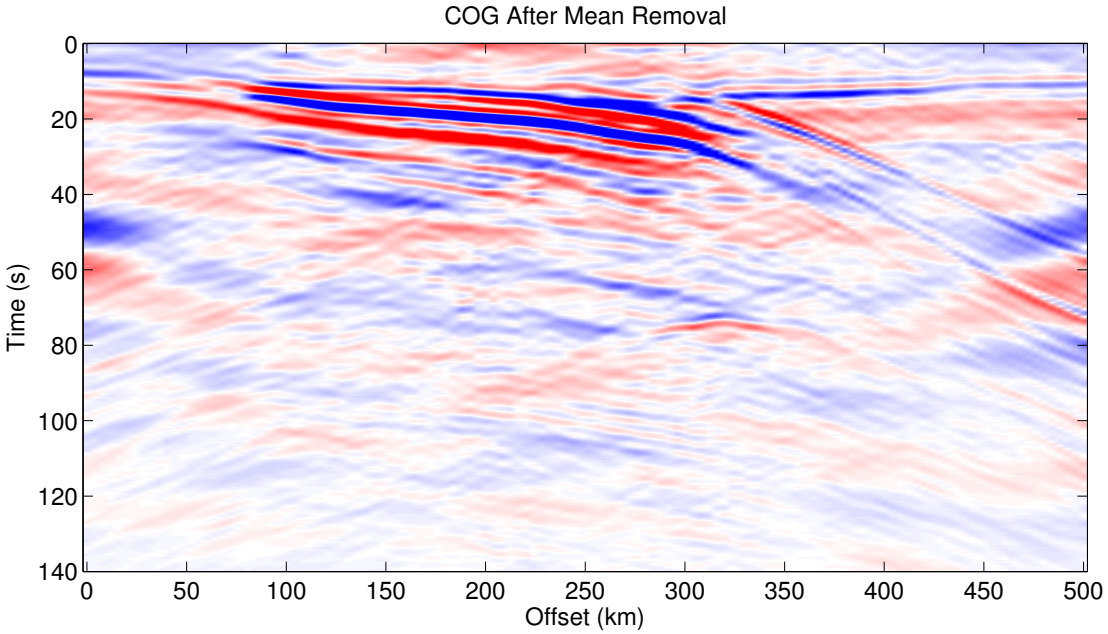

Figure 4.27: A COG example prior to mean removal. Note the near-perfect removal of the horizontally stratified artifacts.

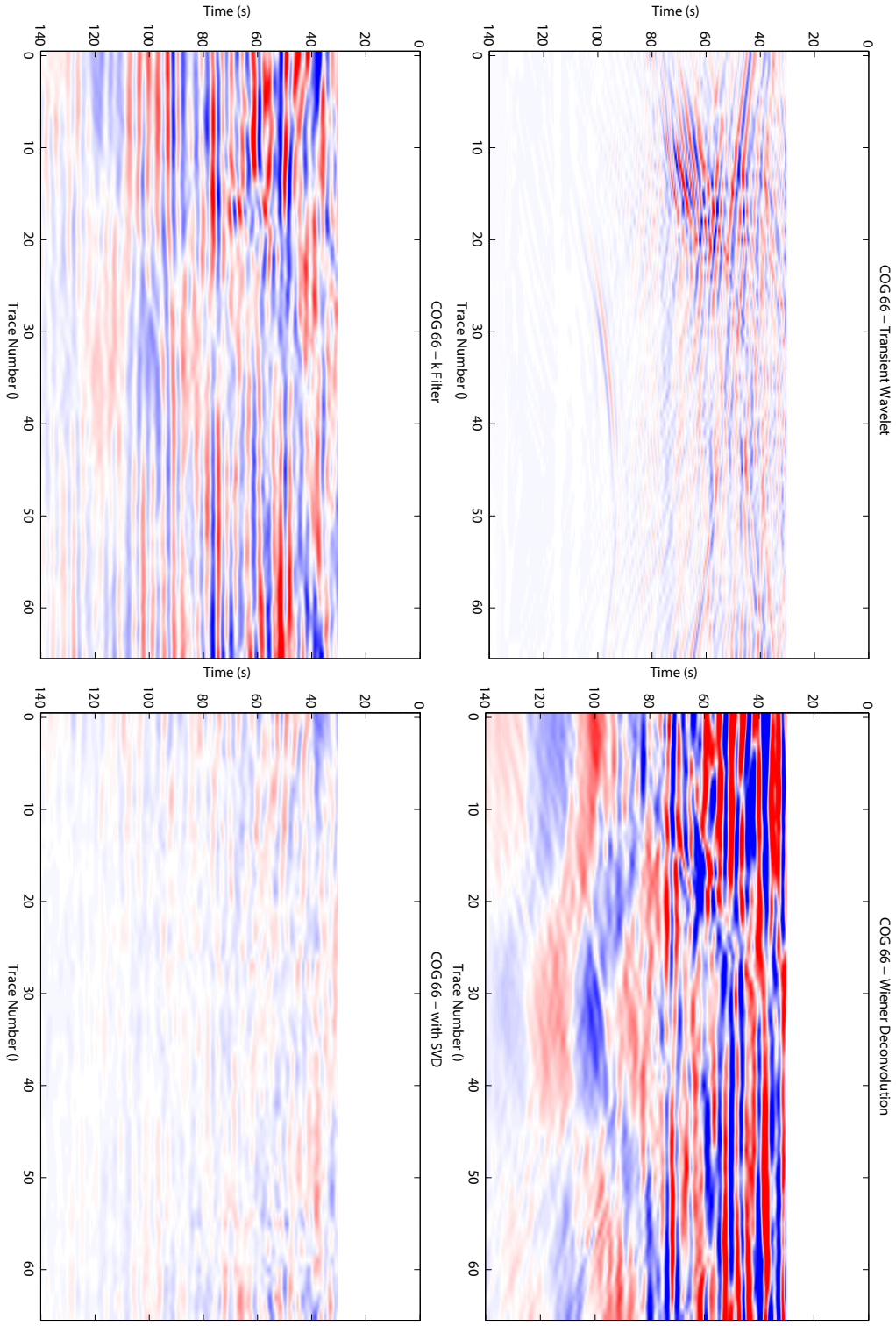

Figure 4.28: Comparison of different processing techniques on COGs. COG 66 corresponds to 60 km offset. The transient wavelet case is taken as the reference model. Energy arriving prior to, and including, the spurious direct arrival is muted for image clarity.

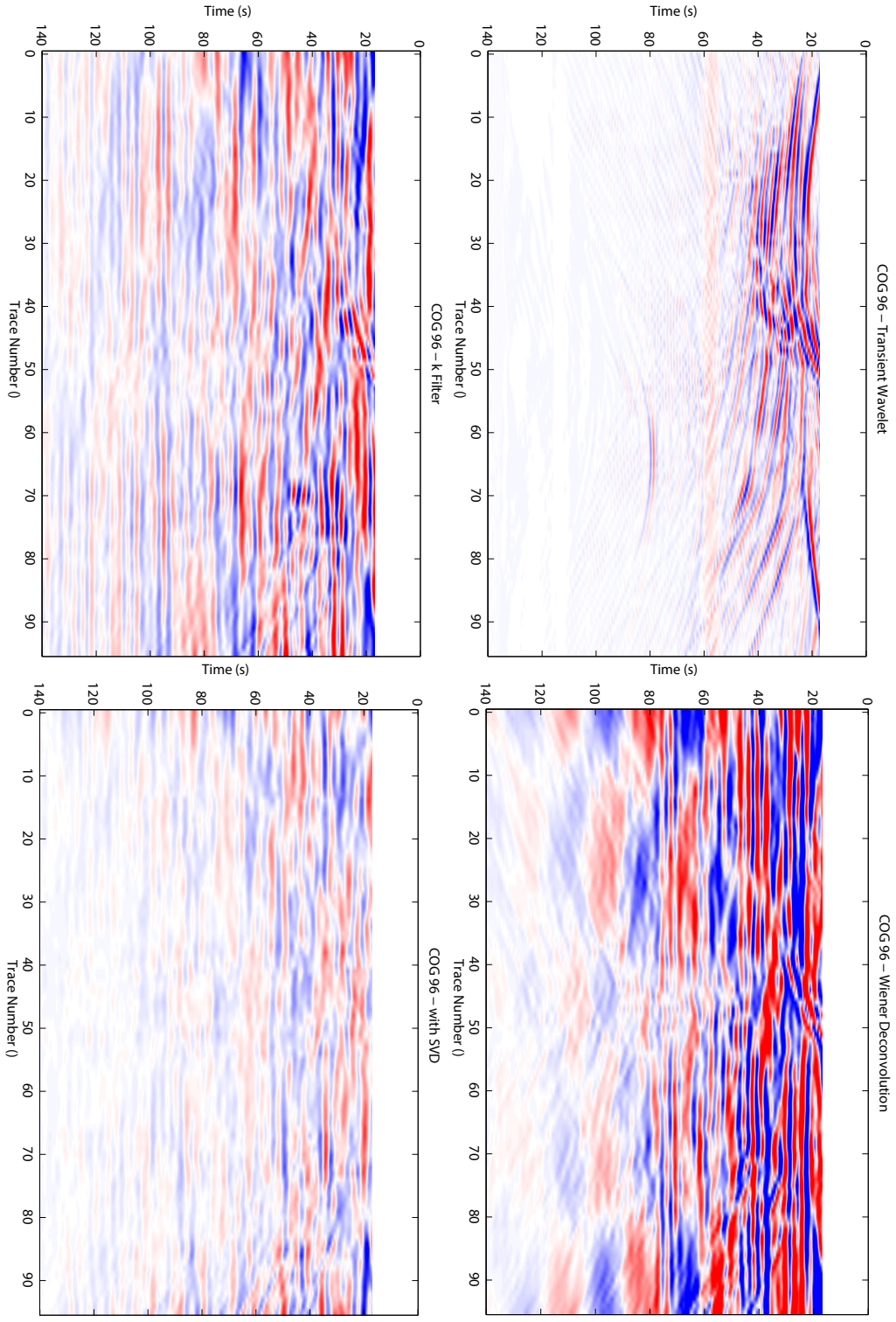

Figure 4.29: Comparison of different processing techniques on COGs. COG 96 corresponds to 30 km offset. The transient wavelet case is taken as the reference model. Energy arriving prior to, and including, the spurious direct arrival is muted for image clarity.

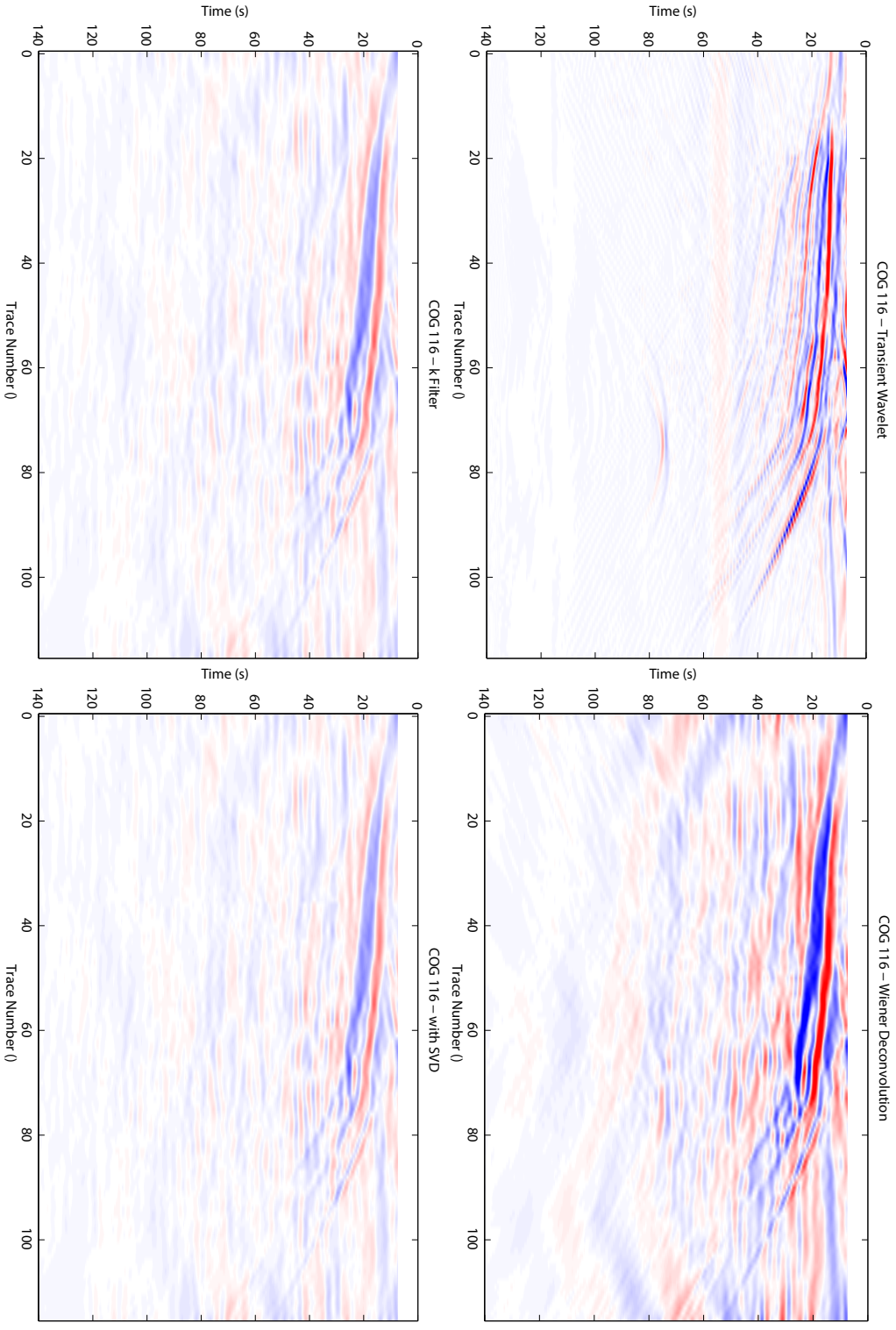

Figure 4.30: Comparison of different processing techniques on COGs. COG 116 corresponds to 10 km offset. The transient wavelet case is taken as the reference model. Energy arriving prior to, and including, the spurious direct arrival is muted for image clarity.

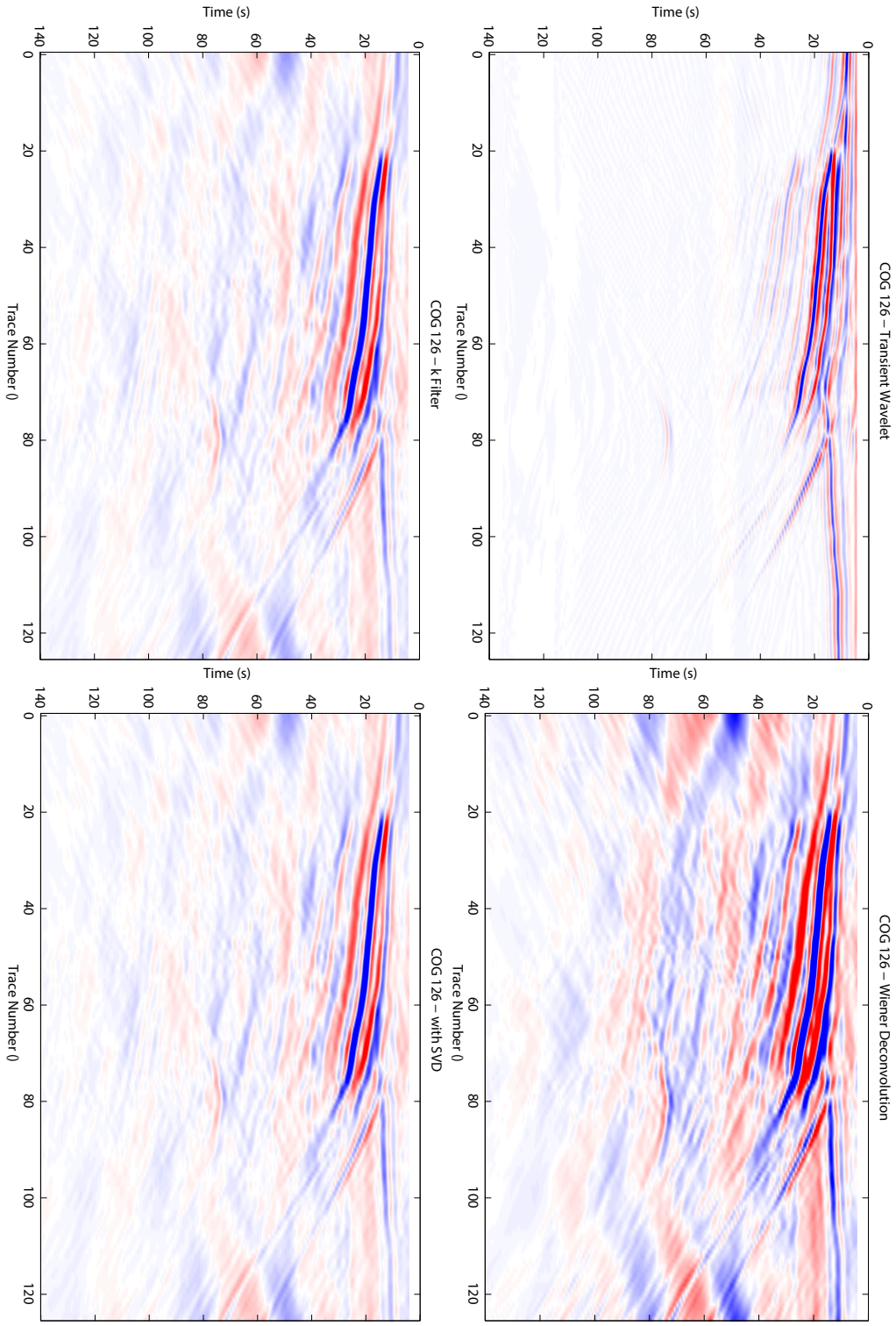

Figure 4.31: Comparison of different processing techniques on COGs. COG 126 corresponds to zero offset. The transient wavelet case is taken as the reference model. Energy arriving prior to, and including, the spurious direct arrival is muted for image clarity.

filter, along with a non-obvious optimal parameter choice, we conclude that wavenumber filtering is an unnecessary processing step.

Lastly, it is difficult to draw a definitive conclusion regarding which remaining option is better; that is, whether Wiener deconvolution followed by whitening brings any advantage over the whitening only case. At the late times, it is clear that the deconvolved dataset appears to remove some of the low frequency undulation from the background. Looking specifically at figure 4.29, at times greater than 80 s, there is a dramatic reduction in the number of horizontally layered features. From the known model, there should be no reflectivity at the corresponding depth. The situation without deconvolution, however, could be misinterpreted to contain physical reflectors. At extremely long offsets, such as those found in figure 4.28, the deconvolved dataset can find reflectors where whitening alone cannot. Toward the 100 s mark, there is a response to the bottom of the slab displayed in the deconvolved dataset. While some curvature is present in the whitening only panel, it is not as clear as the deconvolution panel. For this synthetic case, it appears as though using the trace itself as a filter design for Wiener deconvolution, followed by whitening, produces the best result. The expectation that this technique would result in extra ringiness from spurious cross terms seems unfounded for synthetic data. However, given subtle improvements noted here, testing on the field dataset will be required.

4.6 Imaging

The final goal of this project is to produce a migrated image of the subduction zone in southern Mexico. To determine the best imaging technique to apply to the field dataset, testing on the synthetic dataset is applied. We proceed with the whitened dataset described in the previous section. Migration is implemented by a pre-stack Kirchhoff shot migration code. Each virtual source record is migrated using a 1D velocity model and again with the true 2D velocity model to compare the effects of the different models. The true 2D velocity model is available from the interval velocity model used to create this dataset. Although such a model will not be available in the field data scenario, it is of interest to study the quality of the final image achieved with a theoretically perfect velocity model against a comparatively crude 1D velocity model.

The best migration result was achieved using a migration aperture equal to five station intervals from the output trace position (20 km) and discarding offsets larger than 40 km from the virtual source position. The image we obtain using the 1D velocity model is shown in figure 4.32. Comparing this result to the model in figure 4.1, it is clear that all of the major features are reproduced, even including the abrupt bottom of the slab. There appears to be two artifacts that branch off near the region where the slab begins to dip steeply (near 350 km and 20 s). This dipping feature is not physical, but may exist due to the abrupt truncation of ray parameter sampling at ± 0.120 s/km. This abrupt ray parameter boundary results in a contribution to the SI correlation panel that cannot be interfered with by larger ray parameters according to the continuous integral described in equation 2.1. This results in a contribution from the largest ray parameters available that has no physical basis. Including illumination from larger ray parameters could potentially limit the effect of this artifact. Alternatively, by diminishing the amplitude of traces produced with large ray parameters, it is possible this artifact would be reduced or removed.

The image we obtain using the true RMS velocity model is shown in figure 4.33. The migration differences between the 1D velocity model and the true RMS velocity model are minimal. The same physical features appear in both, and the clarity of these features is arguably identical.

One slight difference is present in the bottom of the slab; the true velocity model appears to properly limit its horizontal extent, whereas the 1D velocity case smears the large offset portion slightly upward in the time axis.

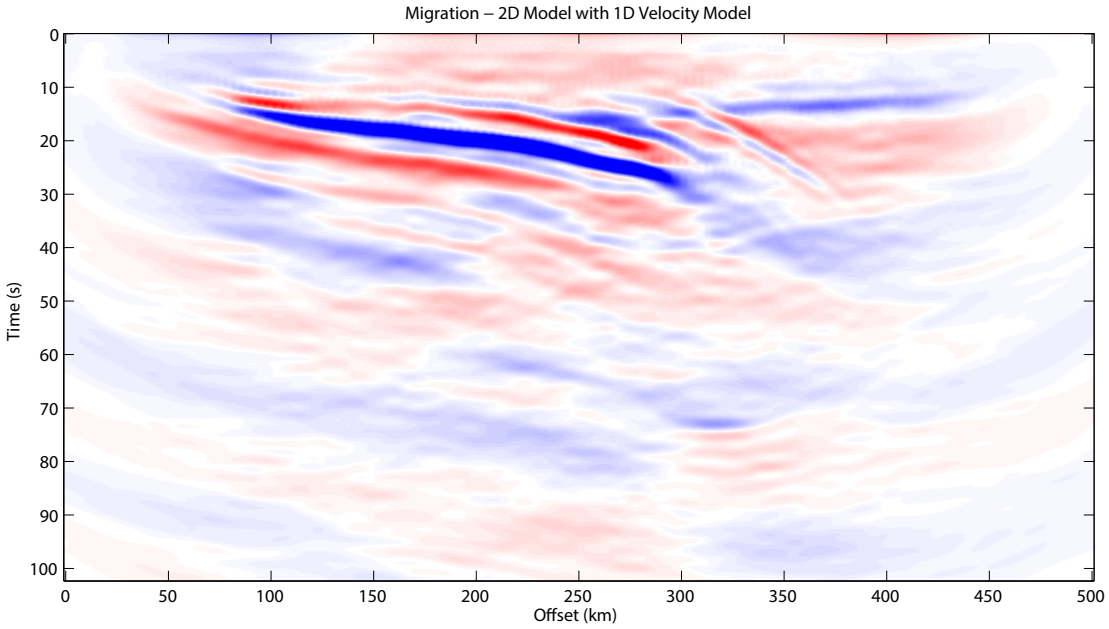

Figure 4.32: The migration result of the 2D dataset using a 1D velocity model.

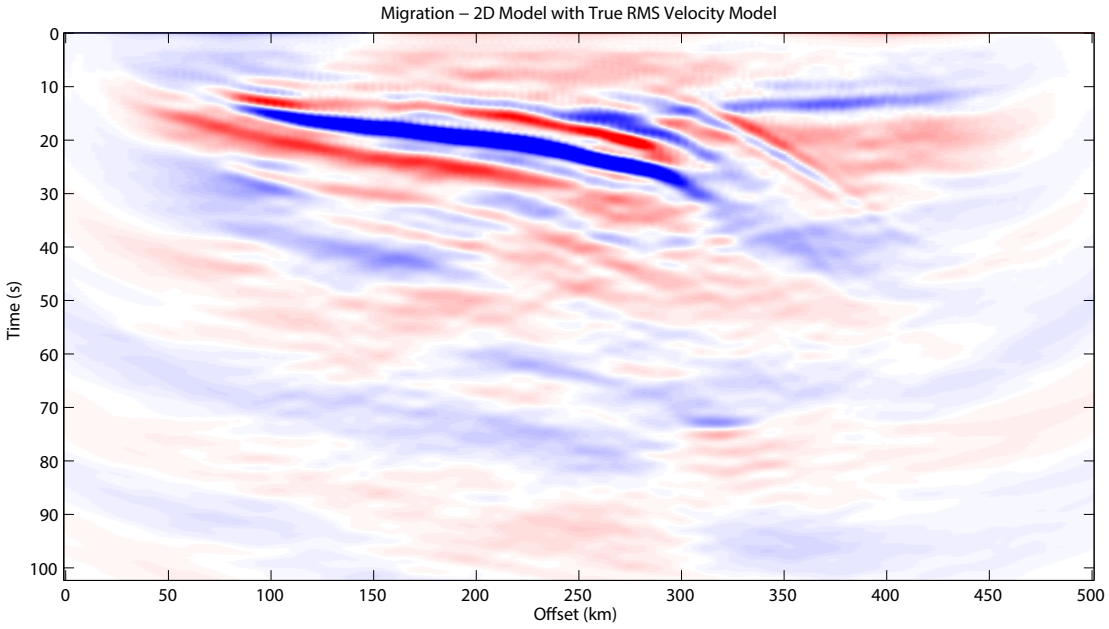

Figure 4.33: The migration result of the 2D dataset using the true RMS velocity model.

We proceed with the 1D velocity model to make a time-to-depth conversion of the migration result. The conversion is applied in a trace by trace manner; this is the same velocity model used in migration. The final result is trimmed to the primary area of interest for viewing (Figure 4.34) and can be directly compared to the interval velocity model used in the forward modelling stage (Figure 4.35). The first reflector is still relatively obscured, but further processing to remove the low frequency oscillations introduced by previous steps could lead to improvement. Regardless, the processing flow determined through the 1D and 2D modelling is capable of accurately producing a migrated image of the model subduction zone.

While the field data processing and results will be discussed in the following chapter, a final test is performed in the 2D case. We wish to image the 2D model using only ray parameters that are actually available in the field dataset. The ray parameter sampling available in the field dataset is determined using a global ray tracing algorithm dependant on the selected S phase (i.e. PS phase will sample a different ray parameter than an S or SKS phase, see figure 2.1). Knowing the sampling available in the field case, the 2D transmission responses are decimated such that only ray parameters available in the field case are available in the 2D model. Ray parameters in the field dataset are rounded to the nearest ray parameter values available in the 2D modelling. This establishes a set of "bins" which are either sampled or not sampled in the field case. Non-sampled bins are then discarded from the synthetic dataset. Although over forty phases are available in the field dataset, many sample similar ray parameters. This results in a diminished dataset with only 16 unique ray parameters for the synthetic transmission responses. This concept, along with the tally of field data and 2D model ray parameters, is illustrated in figure 4.36. Proceeding through the previously established processing flow, the migrated result is given in figure 4.37 with the 1D velocity model used. Although the image quality has been reduced, the same major features present in the ideally sampled scenario are present.

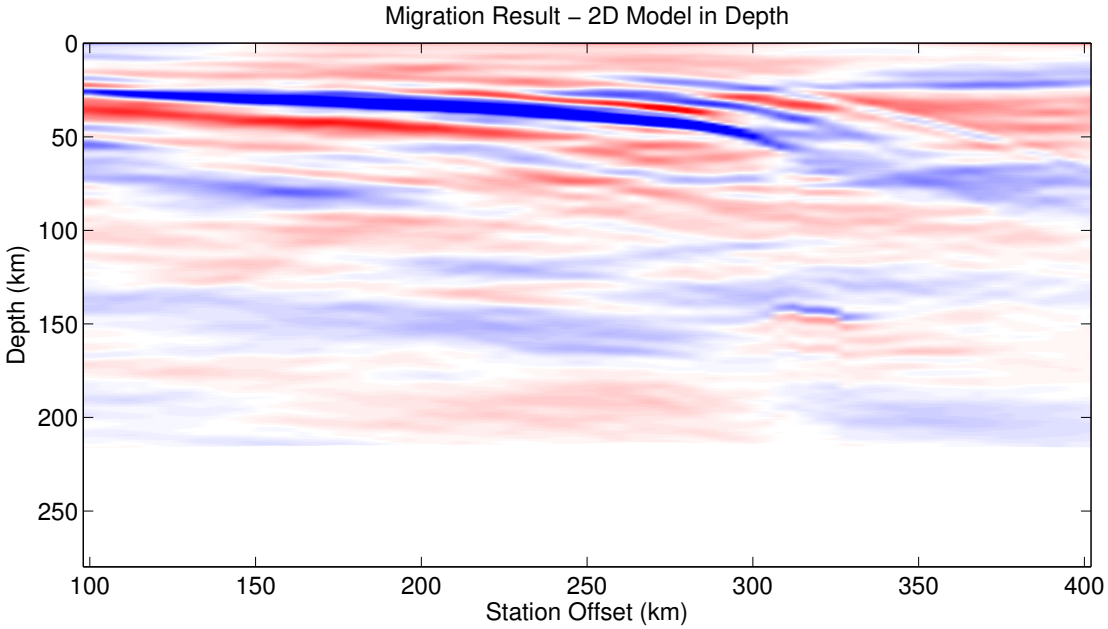

Figure 4.34: Final migration result of the 2D model subduction zone.

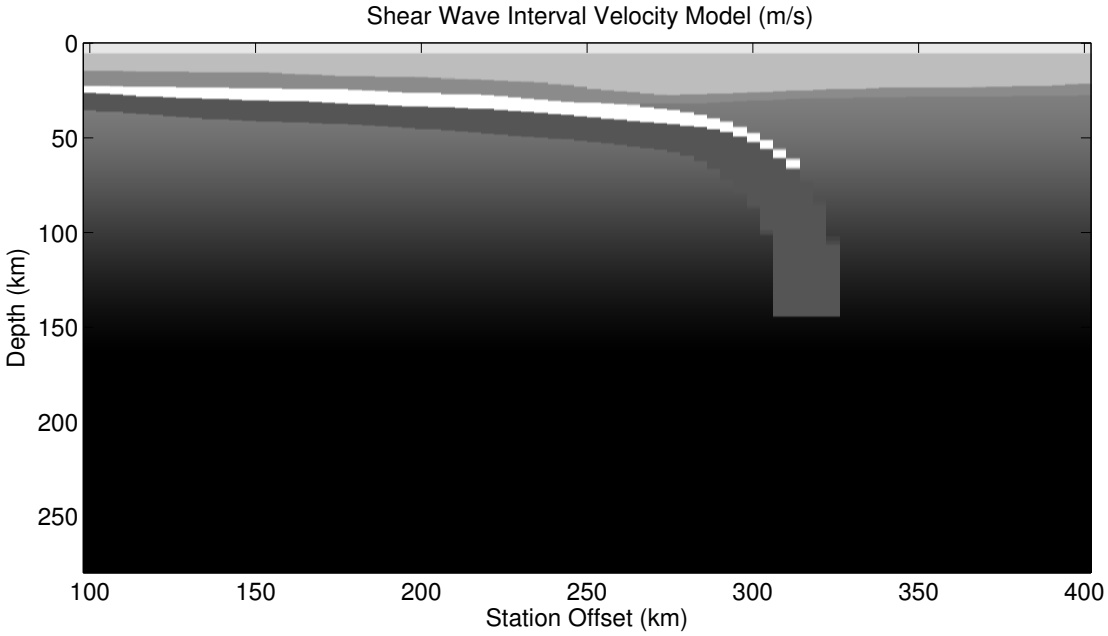

Figure 4.35: Subduction zone model for comparison with figure 4.34.

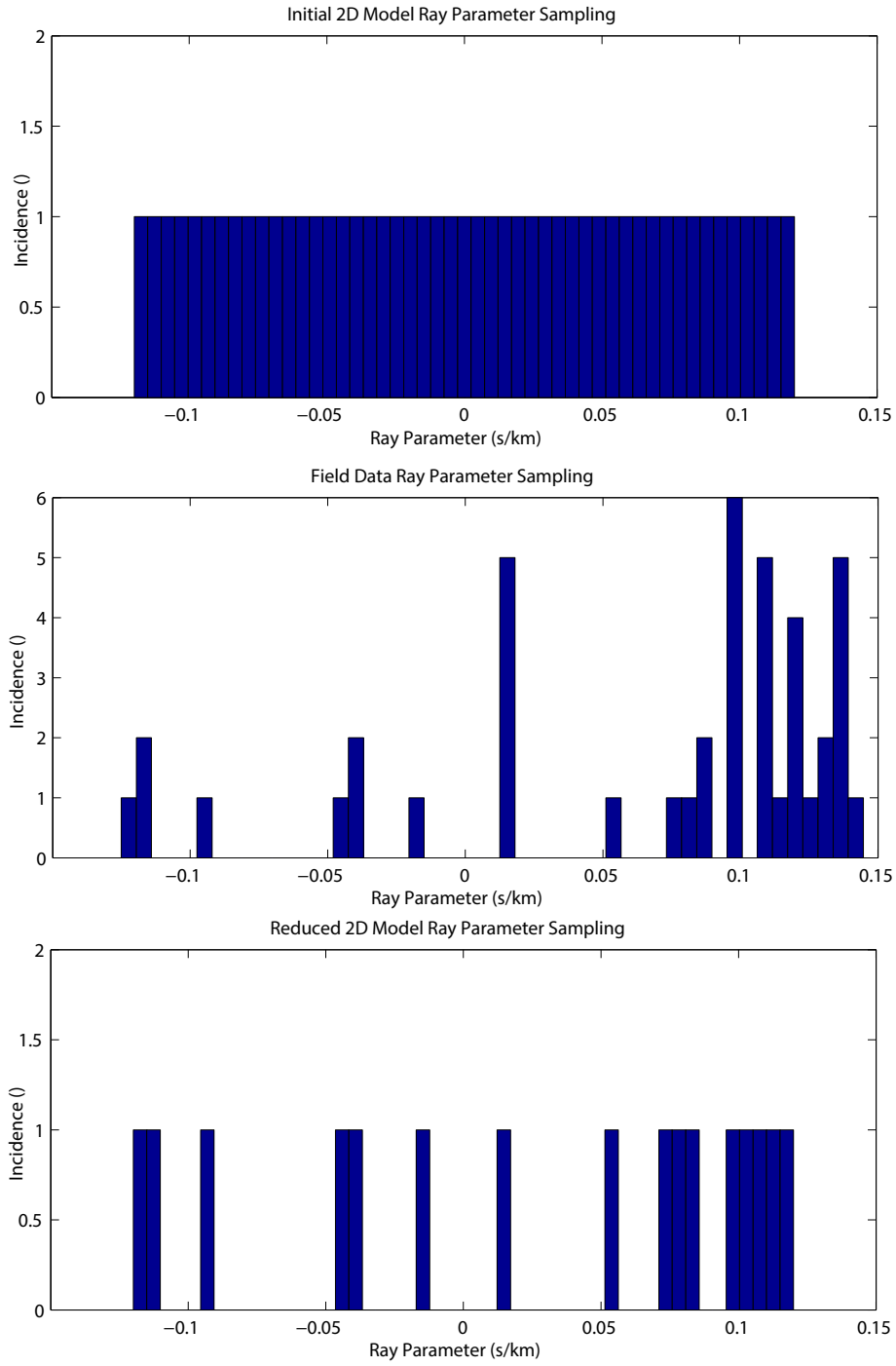

Figure 4.36: The top panel shows the ray parameter sampling available for the 2D modelling. The central panel shows the actual ray parameter sampling of the field dataset sorted into the same bins as the 2D modelling. The final panel shows the reduced modelling case where only ray parameter bins sampled by the field data are available for the forward modelling.

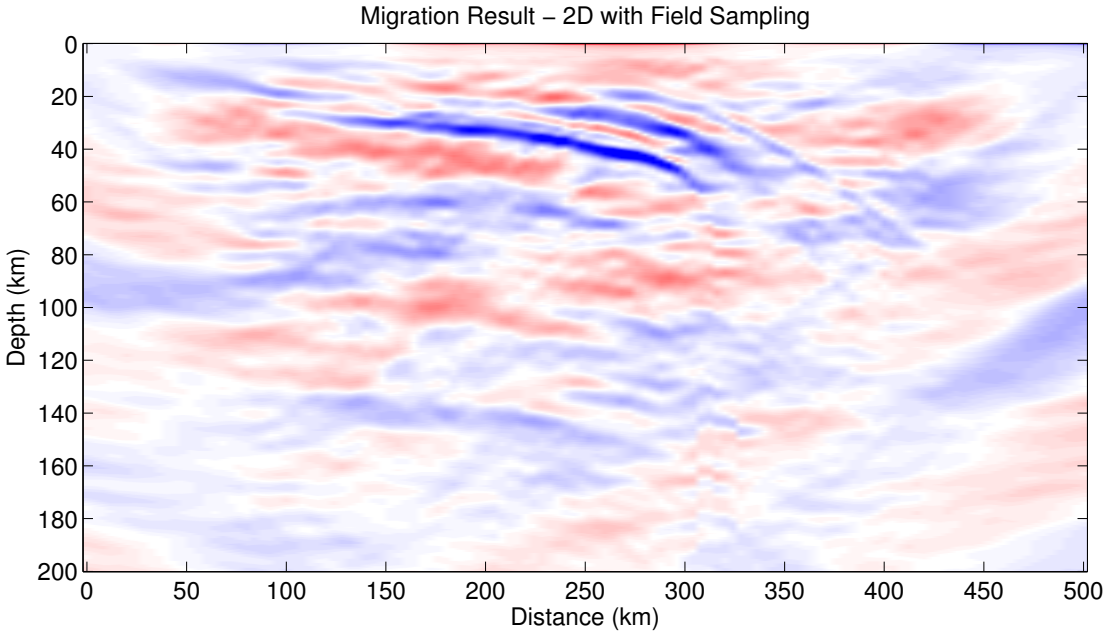

Figure 4.37: The 2D model migration result produced with the field dataset ray parameter sampling.

Chapter 5

Field Data

5.1 MASE and the Dataset

To reiterate the introduction, the field dataset selected for analysis comes from the MASE array in southern Mexico. There are 100 station locations with approximately 5 km separation. The location of each station is depicted in figure 5.1. This temporary array was active for a period of approximately two years, the retrieved data spans from January 2006 until June 2007 as available on the IRIS database.

During this time frame, many thousands of earthquakes have occurred; however, for the purpose of imaging Mexico's subsurface, restrictions are necessary to limit the dataset to earthquakes that make a meaningful contribution toward this objective. For SI to be applied in our configuration, it is critical that the travel path of the plane wave impinging at the receivers propagate from one station and reflect to other stations on the surface. If the plane wave approaches the array perpendicularly, the energy will not "bounce" between stations and will not sample the subsurface in between. This restricts the available earthquakes to those that are near the line bisecting the stations of the array. We limit our search to earthquake epicentres that occur within an azimuth of 30 degrees of the orientation of that bisecting line. However, to supplement the number of recordings available, we expand the 30 degree criteria to also accept large magnitude earthquakes with very low ray parameters. With very low ray parameters, sampling between stations is possible even if the event does not locate near the great circle path. Not all earthquakes are created equal in terms of energy released; by manually sorting through many recordings, a minimum moment magnitude (M_w) of 5.5 was required to provide sufficient energy at the array. A filter was applied to automatically discard lower magnitude events, which further reduced the number of remaining recordings. The earthquake epicentres available in the final dataset are shown in figure 5.2; note the proximity to the great circle path through the MASE array depicted by the red dashed line.

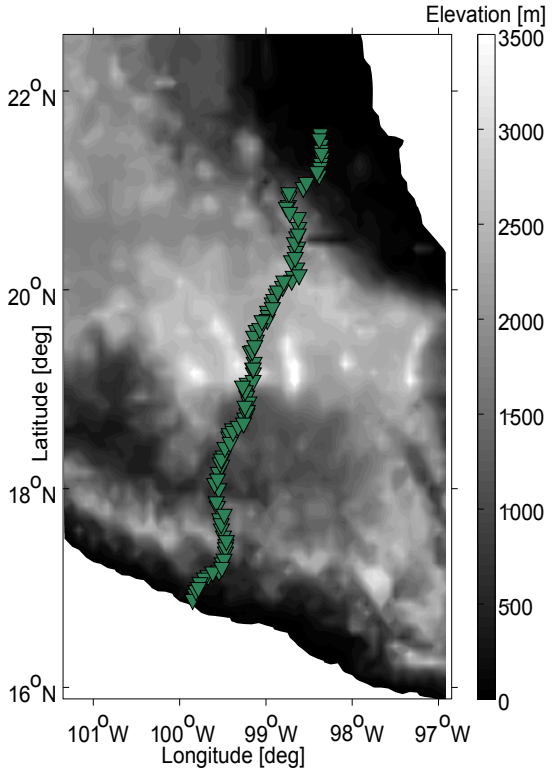

Figure 5.1: Latitude and longitude of the MASE array stations.

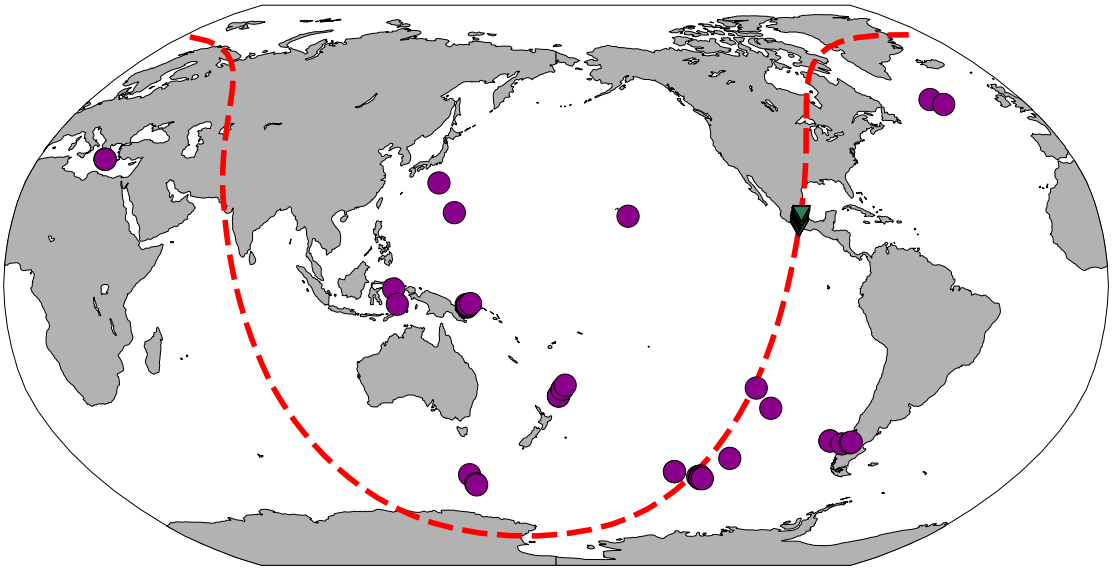

Figure 5.2: Depiction of the earthquake locations that contribute S phase transmission responses to the dataset. While most epicentre locations occur near the great circle path through the MASE array, large magnitude events which sample low ray parameters away from the line are also included.

5.2 Processing and SI

With our imaging method established in the previous chapters, we begin constructing a suitable field dataset. We begin by windowing individual S phase responses with sufficient signal to noise quality from the dataset retrieved. In total, we retrieve 43 unique phases. As mentioned in chapter 2, the contribution to the total number of phases comes from both S_V and S_H transmission responses. Receiver coordinates are rotated at source direct P energy maps primarily to the vertical component. This also isolates the majority of the S energy to the radial and transverse components. SKS and PS phases map to the radial receiver component; S, SS, and ScS phases can be detected on both the radial and transverse components. As anticipated, decomposition further improved the isolation of the S phases. The greatest effect is evident in large ray parameter transmission responses; decomposition is applied according to the process discussed in section 4.3.1. The receiver component used while windowing the S phases determines which field is isolated, either S_V or S_H.

We discussed that anisotropy is not taken into account because it is expected to make a small contribution to the final image resolution. The recent paper by Stubailo et al. (2012) notes that regional shear wave velocity variations of about 300 m/s are present in some regions along the MASE array between the crust and mantle. A sample calculation shows that for a feature 100 km thick experiencing maximum anisotropy from a base velocity of 4000 m/s, we expect a maximum two-way travel time difference between S_V and S_H energy to be approximately 3.5 seconds. Given the majority of the imaging energy is focused in the range from 0.05 to 0.20 Hz, this anisotropy is anticipated to make a small effect in data quality.

A typical windowed S phase transmission response is depicted below in figure 5.4. Note that although 100 stations were available in total, many traces were discarded due to poor quality. The windowed phases are then low pass filtered and decimated from a 0.01 s to 0.25 s sample interval. This reduces the Nyquist frequency to 2 Hz, but the dataset contains little imaging energy content above 0.5 Hz. Any high frequencies present in the records are attributed to local noise sources. Whitening is applied to the interval from 0.01 to 0.40 Hz. Conveniently, the instrument response is flat over both the amplitude and phase spectra in this band, thus an instrument correction is not applied.

A correction to account for topographic variation is made at this point. In order to account for the additional travel time to elevated stations the value of the true ray parameter and apparent ray parameter is required. The true ray parameter is calculated by ray tracing as a function of epicentre location to the centre of the MASE array; this is the path the individual phases take directly from the earthquake event to the MASE stations. Apparent ray parameter is defined as the plane wave ray parameter as seen by the array; thus, it is a projection of the actual ray parameter to the vector spanned by the array. Note, the apparent ray parameter is always a smaller value than the true ray parameter; this is purely a consequence of geometry. Once these values are determined, we correct for the topography and redatum the arrivals to a fixed elevation. A time shift is applied to each trace according to the extra travel time through the subsurface for elevated stations according to the apparent ray parameter. As the nuances of the near surface velocity are unknown, a bulk shear wave velocity of 1800 m/s is applied in the corrections.

A second correction is made to shift the arrival time of energy received at the array to travel times expected if sampled by an event on the great circle path through the array. A simple thought experiment can illustrate the concept applied here. An event arriving perpendicular to

the array will appear to have infinite velocity. Similarly, an event arriving off of the great circle path through the array will have an increased apparent velocity compared to an event located on the great circle path. Therefore, an event occurring on the great circle path through the array to have a greater move out than an event off of this path. In practise, we extract the arrival time of the energy from the first station encountered by the approaching plane wave and shift the subsequent traces along the plane wave travel path according to the true ray parameter and distance to the subsequent station. As such, this correction assumes that the structure encountered outside of the plane of the array is the same as the structure in plane. The effect achieved is subtle, epicentres up to 25° from the great circle path have apparent ray parameters within ten percent of the true ray parameter, resulting in a small time shift. This correction ensures a geometrically correct travel time between stations.

Next, interpolation is applied to replace for traces removed in the transmission response. A linear interpolation algorithm is used to replace these traces. Not all traces are interpolated if the gap resulting from removed traces could result in aliasing upon interpolation. This is determined by calculating the spatial Nyquist frequency from the frequency content present in the data. If aliasing is a risk, the trace remains empty. Figure 5.3 shows the incidence of traces before and after interpolation by their station number. Recall, a total of 43 transmission responses were available from the dataset; thus the maximum traces available for a given receiver position 43 occurrences. Prior to interpolation, some receiver positions are entirely absent of recorded data. These stations typically exhibited a high level of noise or were faulty due to some unknown cause. Fortunately, the majority of traces were interpolated without aliasing. Note, if the end of line receivers were lacking data, the adjacent trace is copied to that position. Although not an ideal solution, trace to trace character of adjacent receiver positions is typically consistent. Travel time shifts (as described above) are applied to these end of line traces.

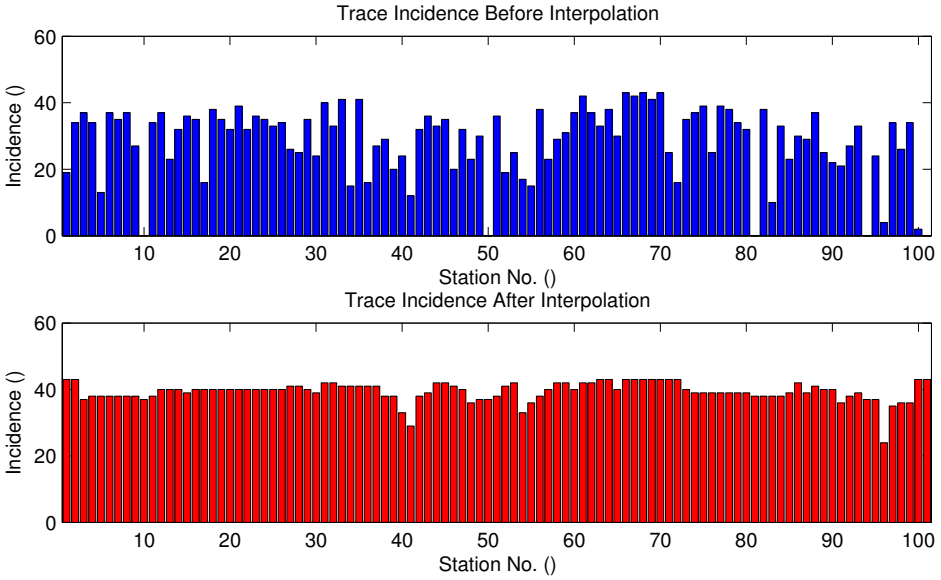

Figure 5.3: Trace incidence before and after interpolation is applied to the transmission responses.

A final geometry correction is applied prior to SI. Although not required for SI application, we desire regular sampling along the span of the array and therefore interpolate each transmission response to a regularized interval. The total linear distance covered between the first

and last station is approximately 540 km; after regularization, the trace spacing becomes 5.4 km. The cumulative effect of the whitening, topography correction, travel time correction, trace interpolation, and geometry regularization is shown in figure 5.5. This can be compared to the pre-corrections transmission response in figure 5.4.

The SI implementation employed for the field dataset is identical to the technique discussed in chapter 4. Each phase in our dataset contributes to the final SI virtual response as described in the right hand side of equation 2.2. A typical virtual source record is shown in full in figure 5.6. As with the synthetic data retrievals at large offsets are of little imaging value. Offsets larger than 100 km are of poor quality and are therefore discarded. Additionally, a top mute and mean subtraction are applied to the virtual source records reordered to common-offset gathers, as discussed in section 4.6. The final result of this post-SI processing is shown in panel (b) of figure 5.7. Figure 5.7 shows the scenario where a virtual source is produced at the position denoted by the red star in panel (a). By discarding long offsets (greater than 100 km), the gold encircled area shows the receivers that contribute to the traces in panel (b).

5.3 Imaging

With the virtual source records prepared, the final stage of the project was to proceed to migration. The same Kirchhoff pre-stack shot migration algorithm discussed in section 4.6 is employed here. Although a high quality migration result was achieved with a variety of parameters in the 2D model, extensive testing was required to determine the best image quality achievable with the field dataset. Tests were conducted to determine the best parameter for migration aperture, maximum offset, optimal bandwidth, and velocity model. As mentioned in the previous discussion, the best results were obtained with a bandwidth whitened to a maximum of 0.40 Hz and including a maximum offset of 100 km. The testing also revealed that the crispest images are obtained with a maximum migration aperture of 10 station intervals (54 km). The overall quality of the data did not allow for a velocity analysis using semblance plots and iterative velocity picking; however, a satisfactory image was produced by permuting velocity values found in the Preliminary Reference Earth Model (PREM) by Dziewonski and Anderson (1981). The time migration is presented in figure 5.8. With a depth conversion according to the velocity model used in the migration, the final depth section of the Cocos subduction zone below the MASE array in southern Mexico is presented in figure 5.9. Note, in all figures, distance increases toward the north direction. The town of Acapulco is located near 0 km, Mexico City locates near the 300 km position, and Tempoal at the end of the profile.

The result of the migration is an interesting for a few reasons. At 25 km depth, a strong positive reflector is present from 0-250 km offset. This feature is likely the crust-mantle contact. Toward the centre of the profile, significant depth increase of this contact occurs; this corresponds to the crustal thickening associated with the mountain range north of Mexico City. At greater depths, the profile shows relatively planar layering for the first 200 km. At the southern side of the array, the Cocos plate subducts horizontally below the Mexican continental crust. At approximately 225 km offset and 80 km depth, a slight upturn in the horizontal layering is noted. It appears that a hinge has formed along the subducting Cocos plate, after which greater offsets show a loss of strong reflectivity. This region is where the Cocos plate is interpreted to dip steeply into the mantle and perhaps detach from the remaining horizontally subducting part. Again, the interpretation by (Pérez-Campos et al., 2008) may be referred to for comparison with the results obtained here. Along the entire profile, there appears to be a general dipping trend south to

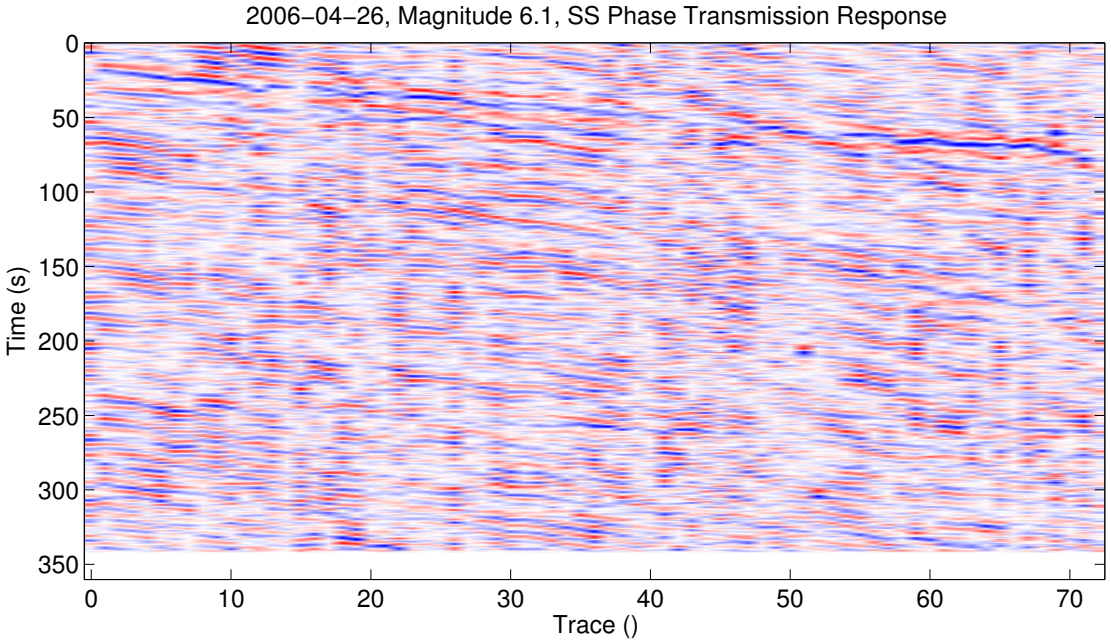

Figure 5.4: A typical SS phase transmission response retrieved from the field dataset. The horizontal axis shows the number of traces available (of 100) after discarding poor quality traces.

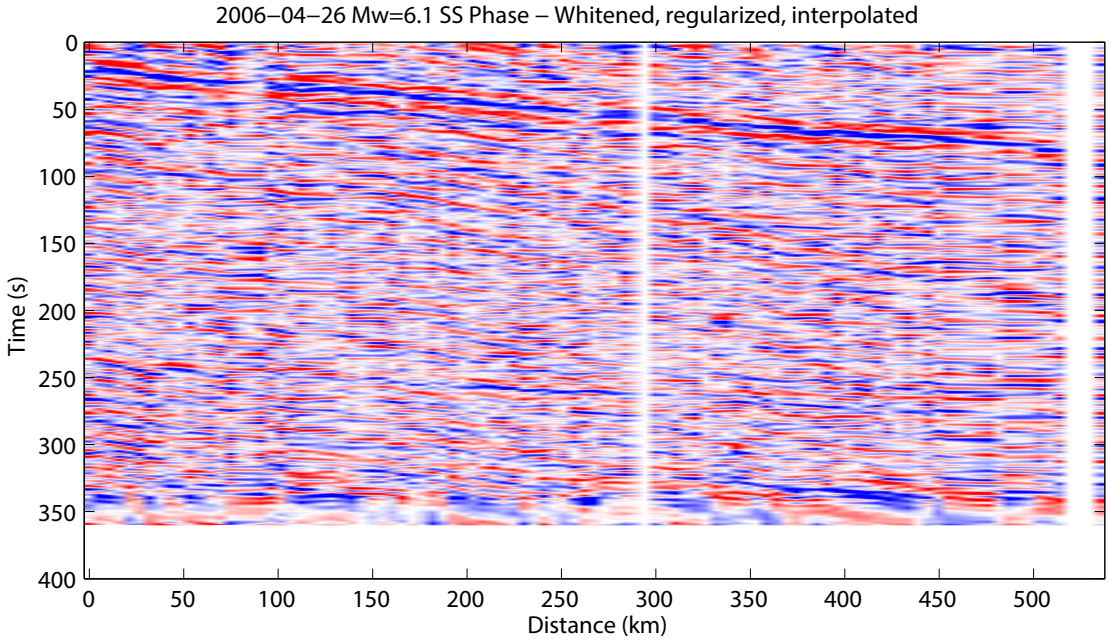

Figure 5.5: The same SS phase transmission response depicted in figure 5.4 after processing steps to prepare for SI are applied. Here, the horizontal axis shows the regularized station spacing.

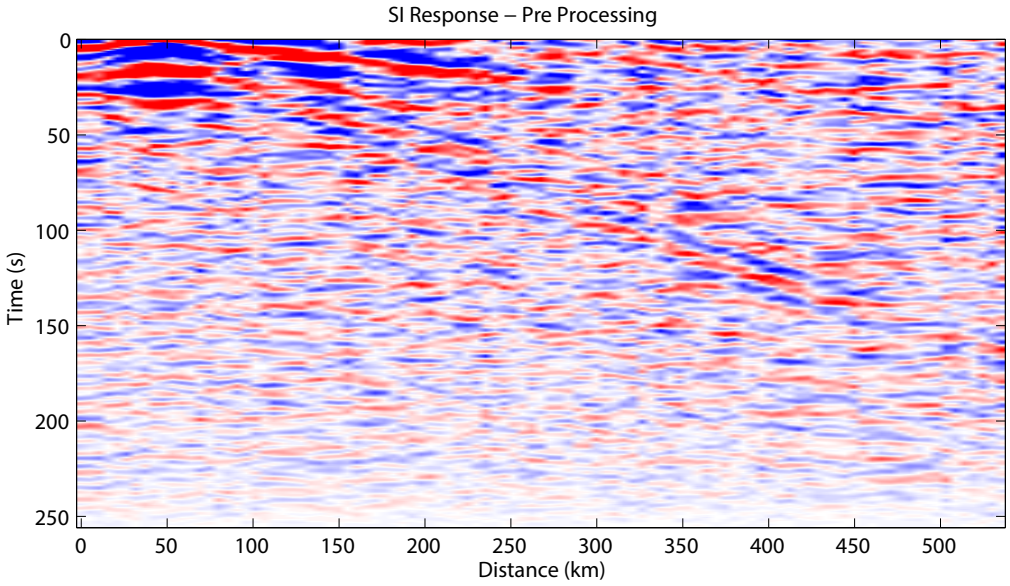

Figure 5.6: A virtual source record produced for a source located at 54 km offset. The low frequency reverberation will be removed in the COG. The spurious direct arrival (and preceding energy) will be removed with a top mute.

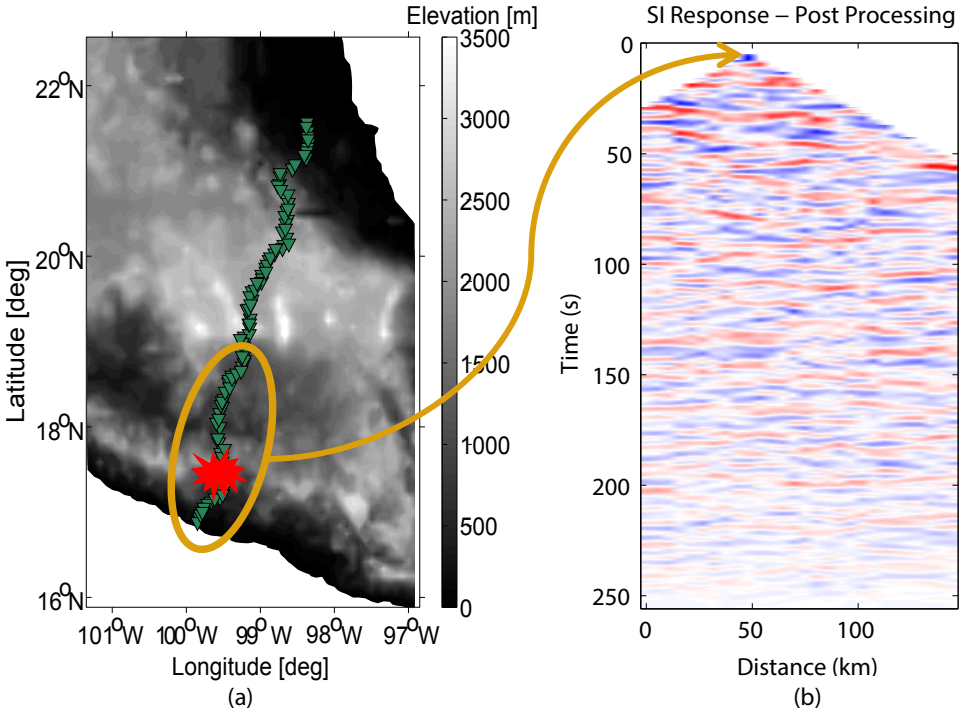

Figure 5.7: Panel (a) depicts a scenario where a receiver at 54 km acts as a virtual source to the regularized array. Panel (b) depicts the virtual source record in figure 5.6 after post-SI processing. Applying a top mute and removing the low frequency reverberation has been applied to the recording.

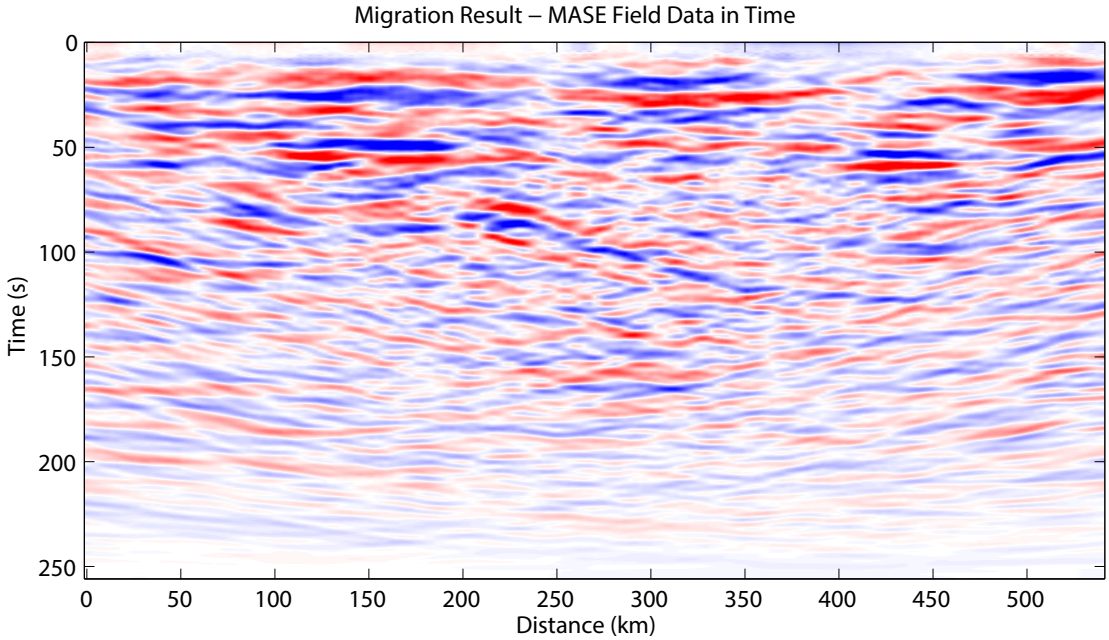

Figure 5.8: The final time migration result achieved from the MASE dataset.

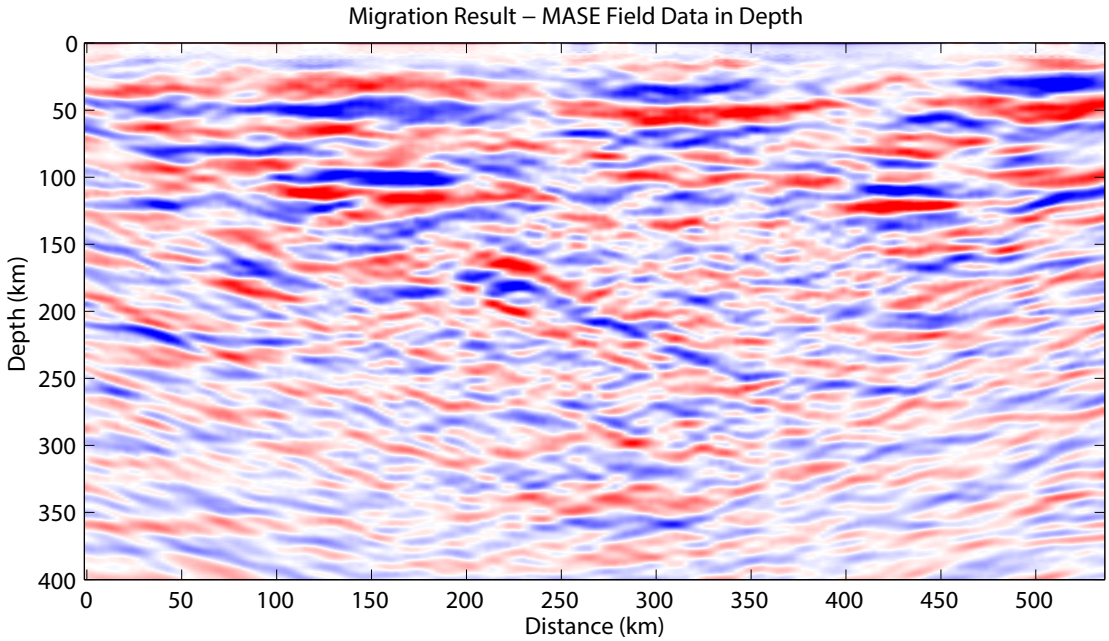

Figure 5.9: The final depth migration result achieved from the MASE dataset

north at greater depths. Toward the largest offset (northernmost section), we resume horizontal reflectivity. This area corresponds to the oldest continental crust of Mexico and is relatively free of the deformation experienced by preceding areas.

As southern Mexico is famous for its extensive (and often destructive) seismicity, we plot the last 40 year's worth of earthquakes that occur within 20 km lateral distance to the MASE array in figure 5.10. Two clusters dominate the image; one from the coastal region (at 0 km) to approximately 150 km inland and another from 250 km to 350 km. The first region (0-150 km) corresponds to the region where subduction occurs in a nearly horizontal fashion and the second region occurs in the Trans Mexican Volcanic Belt (TMVB) (Pérez-Campos et al., 2008). Curiously, between these two clusters is where the slab progresses from near horizontal to steep dip, yet seems to lack seismicity. The plate is moving here, but the absence of seismicity may be attributed to slow-slip events and non-volcanic tremor (Payero et al., 2008).

A final plot is generated with a tomography overlay (Figure 5.11). The tomography result comes from inverting a worldwide dataset of P-wave arrival times (Burdick et al., 2010). The low velocity anomaly below Mexico City colocates with a strong seismic attenuation structure noted in literature immediately below the TMVB (Chen and Clayton, 2009). Lastly, we discuss the dipping feature imaged beginning at 175 km depth and 200 km offset. This dipping feature occurs right in the middle of the positive velocity anomaly according to the AK135 model (Kennett et al., 1995). Although this feature does not appear in existing geological interpretations of the region, it is present in this dataset regardless of migration parameters selected. Modern tomography studies with higher resolution, which focus specifically on this region, determine that the subducting slab dips quite steeply (up to 74 degrees) in this area. Yet given the horizontal extent of this feature, it would appear to transect modern interpretations of the slab location (Husker and Davis, 2009). The exact implication of this dipping feature is uncertain; perhaps it is a relic of mantle material with a significantly lower velocity, or perhaps it is a section of melt within the subducting slab itself. It is also possible that this feature is not imaged at the correct dip due to a lack of large ray parameters. Another interpretation could be that it relates to a chemical change present in the asthenosphere resulting in a material property contrast. Regardless, enhancing the image quality of this region would be interesting to further the interpretation of this and other features.

5.4 Discussion

The clarity of the final image is dictated by the illumination available in the dataset and the usable bandwidth retrievable from the individual phases. The limiting case is always the weakest link; if the majority of the phases recorded only include frequencies up to 0.40 Hz, then the theory of SI dictates that this is the upper limit of the usable bandwidth. We cannot whiten a spectrum where frequency content does not exist. The image produced in figure 5.9 is an achievement, but the vertical resolution is limited. A couple of areas for improvement are obvious: a longer period of recording would result in a greater abundance of available phases and thereby improving illumination. Referring again to figure 4.36, the field case is notably sparsely sampled at low ray parameters; filling in this gap could lead to imaging improvements for continuous reflectors. Furthermore, aligning the array with a more seismically active region could improve image quality. While seismically active, the area of Mexico immediately surrounding the array is not sufficient for imaging purposes. As figure 5.2 shows, the great circle path through the MASE array traces through the far south Pacific and into the Indian Ocean. If aligned with the island belts of southeast Asia, it is possible that a vast increase in large amplitude seismic events could

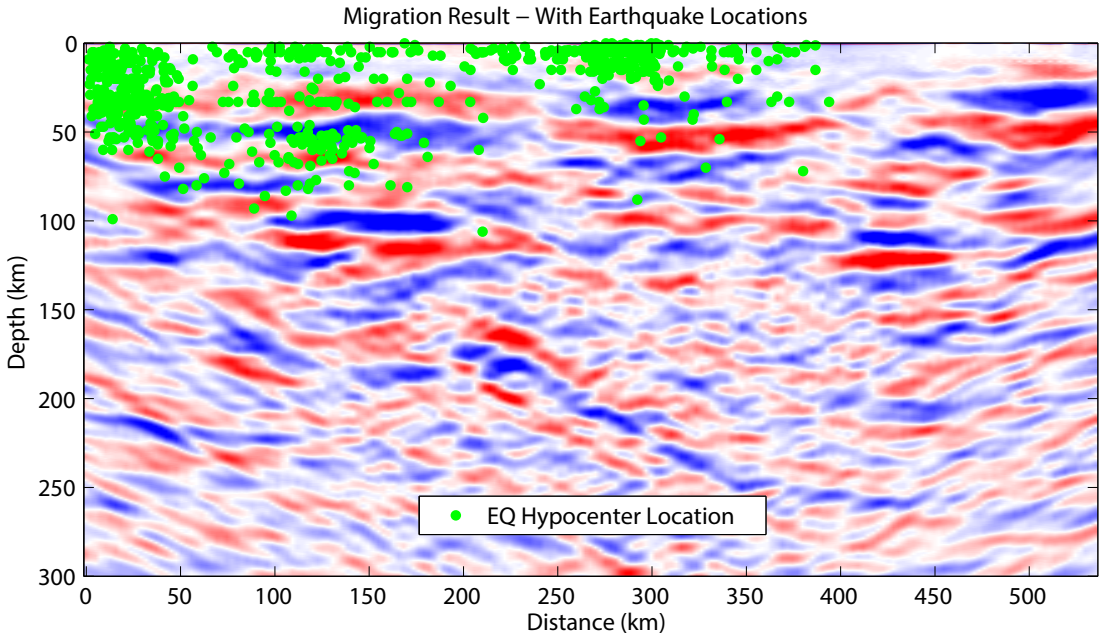

Figure 5.10: Depth migration with earthquake hypocentre locations depicted.

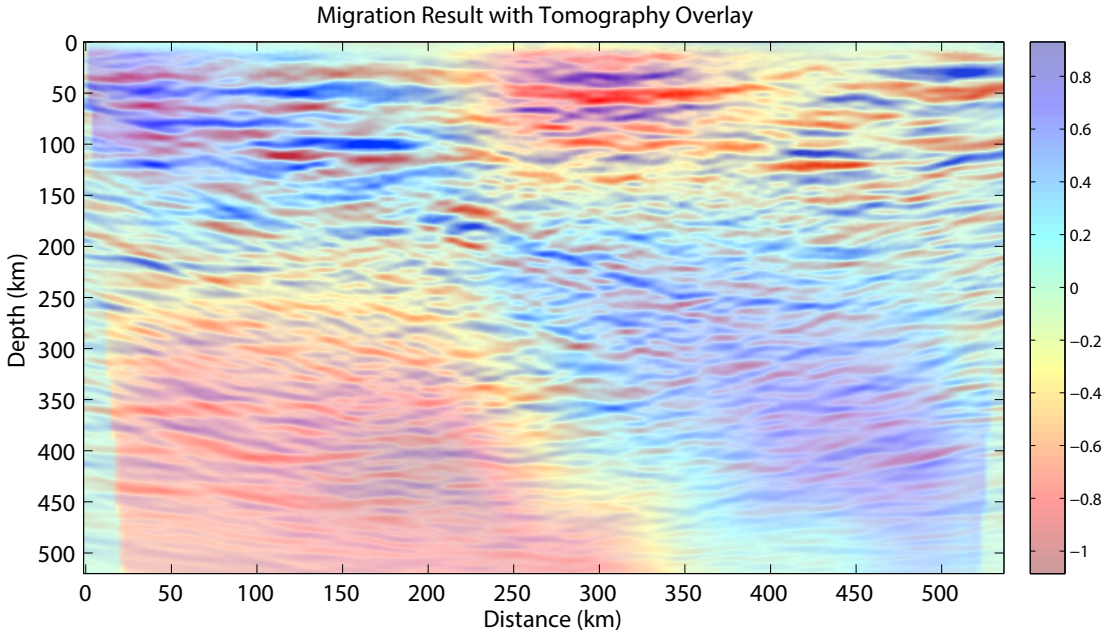

Figure 5.11: Tomography overlay with the depth migration result. Values correspond to percent P-wave velocity perturbations with respect to the AK135 1D earth velocity model.

have been captured. Of course, this different geometry would produce a different 2D profile, but improved interpretations may be possible.

It is possible that further improvements could be made within this dataset itself. Deconvolution tests were fruitless except for the lesson that it does not work elegantly for the two methods employed. This is perhaps not the final conclusion on the subject of deconvolution; there are potentially other techniques that could work better, primarily involving normalization of the trace prior to implementation. The physical properties which give rise to reflectivity ought to approach stationarity in the correlation panel. Preserving this area of stationary phase while discarding the surrounding spurious crosscorrelation terms is desirable for enhancing virtual source record clarity. This was the reason for implementing SVD and wavenumber filtering processes in the 2D modelling chapter. It is possible that a more different technique may lead to subtle improvements at this stage of the processing. Retrieving a P wave reflectivity image may provide other details relating to the section or at least contrast the S wave result. Furthermore, implementing some form of multiple removal may increase resolution. A more accurate velocity model could potentially locate reflectors at more accurate positions, but this effect may be small compared to other improvements.

5.5 Conclusion

With the production of an image of the Cocos subduction zone in southern Mexico, one of the initial goals of the project is reached. By establishing the methodology that can achieve this goal, the other initial objective is complete. It is clear that the shear wave seismic interferometry for lithospheric imaging technique theorized, modelled, and implemented on a field dataset is capable of producing a quality image with interpretable value. Future efforts focusing on signal to noise improvements in the transmission responses with a more thoroughly illuminated dataset could potentially produce an improved image. The features produced in figure 5.9, including the slab hinge point and crust-mantle interface, agrees with the literature from this region (Pérez-Campos et al. (2008); Chen and Clayton (2009); Stubailo et al. (2012)). Application in another region with a well sampled array should be of interest for future work.

Appendix A

Creating Models from Bitmaps

The task of building a complex model in a binary format that works for forward modelling applications can be challenging. Fortunately, at least for the task of input to FDELMODC, we have created a technique that allows a bitmap RGB image to be converted directly into a velocity model. The goal of this appendix is to introduce this idea for future applications. We create an image in any applicable painting program (Photoshop and MS Paint were used here), convert the image using Matlab code, and then convert the output data matrix to SU format. We begin with the following equation;

$$Gr = 0.2989 * R + 0.5870 * G + 0.1140 * B. \tag{A.1}$$

Here, the variable Gr simply refers to a greyscale value assigned by Matlab when converting a RGB bitmap into a greyscale data matrix. The great utility of this is that by creating a colour coded bitmap with the intention of creating a velocity model out of it, one can achieve a precision model through artistic means where each pixel represents a grid point for a forward modelling code. Most techniques available are wonderful for creating simple layered models, but model complexity is often difficult to encode. Three steps are to be followed to use this technique:

1. Create an image where the sum of the RGB terms multiplied by the coefficients in A.1 add up to a value between 1-99. The intention is that this number will be multiplied by 100 to later represent velocity. For example, selecting a value of (200,0,0) for the RGB values, corresponds to a greyscale value of 59.78. In terms of velocity, this can be viewed as 5978 m/s. The use of a image processing program (such as Photoshop) where gradients can be implemented is advantageous; the use of gradients allows for velocity increases that are subtle enough to not produce reflectivity.
2. Convert the image from RGB into grey scale within Matlab; create the respective P, S, and density models; and finally create binary data types out of these files. This can all be achieved by the example script attached below.
3. Bring your files to the environment where FDELMODC exists (Unix or Linux). The data needs to be converted from binary to a Seismic Unix data type with appropriate header fields. This can be automated per the second script (written in BASH scripting).

Taking these steps together allows one to go from a colourful bitmap image (Figure A.1) to a functional model (Figure A.2). Note, it is still critically important that your model is properly sampled to ensure aliasing does not occur. A discussion regarding the necessary sampling in terms of grid spacing, maximum frequency, and model velocities can be found in the manual available for FDELMODC. Further improvements and refinement is certainly possible, but this discussion should provide a sufficient starting point.

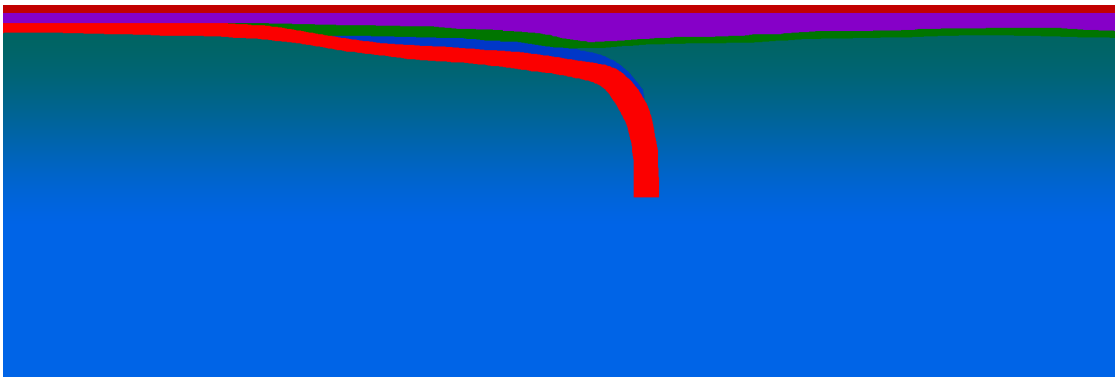

Figure A.1: The colour-coded bitmap version of the model. Note the gradient applied to the underlying layer; by choosing colours according to the described method, it is possible to produce an increasing velocity layer free from reflectivity.

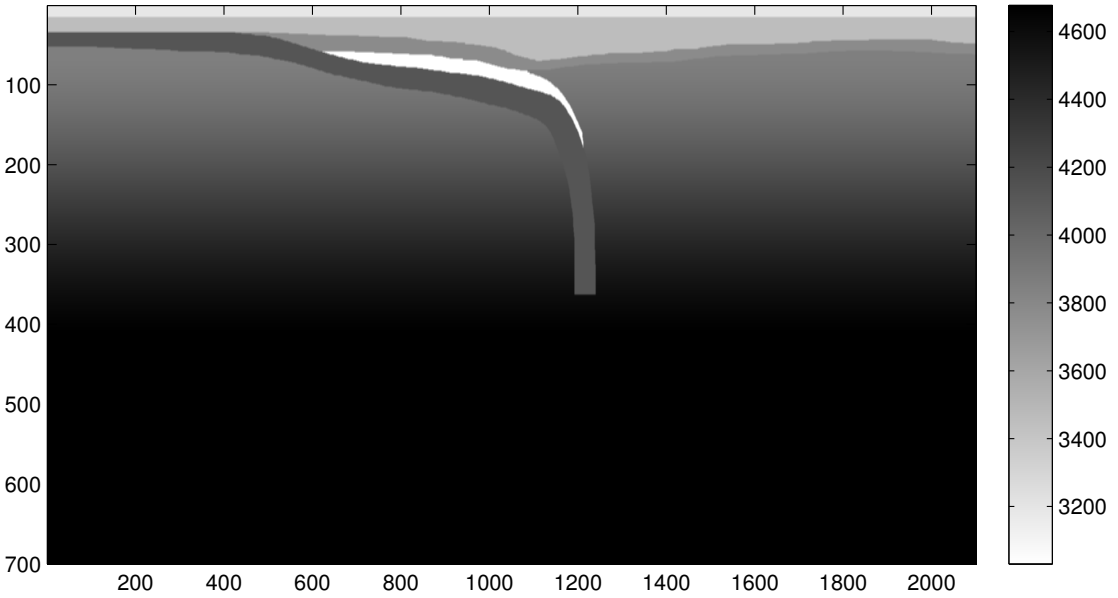

Figure A.2: The grey scale product to be converted to SU type. Axis units are simply number of pixels. 1 pixel equal to 400 m grid intervals were used for the model; the colouration is in terms of shear wave velocity.

Matlab Code: BITMAP to Binary

```
%% Read in Image designed for model conversion

I=imread('subduction_zone_MASE_v5.bmp'); %make model in full dynamic range BMP
I=double(I); %convert from uint8 to double class = higher precision needed next step
J=100*(I(:,:,1)*.2989+I(:,:,2)*.5870+I(:,:,3)*.1140); %values in each cell are now Vp

%Optional filter
h=1/9*ones(3); %this is a 3x3 smoother filter. Can be made larger (i.e. 5x5) by ...
    changing the argument of 'ones'

bits=filter2(h,J,'valid');
J(2:size(bits,1)+1,2:size(bits,2)+1)=bits;

%% Make P Velocity Model
figure(1)
title('P Velocity Model')
cp=round(J);
imagesc(cp);
sizex=size(cp,2);
sizez=size(cp,1);
colormap(flipud(gray(256)));
colorbar;

%% Make S Velocity Model
figure(2)
title('S Velocity Model')
cs=cp*.55; %velocity P-S relation
imagesc(cs)
colormap(flipud(gray(256)));
colorbar;

%% Make Density Model -- Gardner Rule
figure(3)
title('Density Model')
rho=.23*(3.28*cp).^.28; % a modified Gardner rule
imagesc(rho)
colormap(flipud(gray(256)));
colorbar;

%% Convert to Binary types -- to be converted to SU for FDELMODC
fid=fopen('fd_cp_MASE.bin','wb');
fwrite(fid,cp,'float32');
fclose(fid);

fid=fopen('fd_cs_MASE.bin','wb');
fwrite(fid,cs,'float32');
fclose(fid);

fid=fopen('fd_ro_MASE.bin','wb');
fwrite(fid,rho,'float32');
fclose(fid);
```

BASH Script: Binary to SU

```
#!/bin/bash
incp=fd_cp_MASE.bin
outcp=fdmod_cp.su
incs=fd_cs_MASE.bin
outcs=fdmod_cs.su
inro=fd_ro_MASE.bin
outro=fdmod_ro.su

temp=temp.su
nsin=700 #MOD z or t dimension samples
ndin=2100 #MOD x or y or trace dimension number
tridin=130 #CONSTANT not sure -- means something in data type
scalcoin=-1000 #CONSTANT not sure --
timbasin=25 #CONSTANT not sure
trwfin=$[$ndin+1] #CONSTANT trace weighting factor, traces+1
d1in=400 #MOD z dimension interval
d2in=400 #MOD x dimension interval

tracfin=1
tracfinc=1
gxin=$[$d2in*1000]
gxinc=$[$d2in*1000]

suaddhead < $incp > $outcp ns=$nsin #ns is samples in depth/time
sushw < $outcp > $temp key=trid,scalco,timbas,trwf,d1,d2 \
a=$tridin,$scalcoin,$timbasin,$trwfin,$d1in,$d2in
mv $temp $outcp
sushw <$outcp >$temp key=tracf,gx \
a=$tracfin,$gxin c=$tracfinc,$gxinc j=1,1
mv $temp $outcp
suaddhead < $incs > $outcs ns=$nsin #ns is samples in depth/time
sushw < $outcs > $temp key=trid,scalco,timbas,trwf,d1,d2 \
a=$tridin,$scalcoin,$timbasin,$trwfin,$d1in,$d2in
mv $temp $outcs
sushw <$outcs >$temp key=tracf,gx \
a=$tracfin,$gxin c=$tracfinc,$gxinc j=1,1
mv $temp $outcs
suaddhead < $inro > $outro ns=$nsin #ns is samples in depth/time
sushw < $outro > $temp key=trid,scalco,timbas,trwf,d1,d2 \
a=$tridin,$scalcoin,$timbasin,$trwfin,$d1in,$d2in
mv $temp $outro
sushw <$outro >$temp key=tracf,gx \
a=$tracfin,$gxin c=$tracfinc,$gxinc j=1,1
mv $temp $outro
exit
```

Bibliography

Bostock, M. (2004). Green's functions, source signatures, and the normalization of teleseismic wave fields. *Journal of Geophysical Research: Solid Earth (1978–2012)*, 109(B3).

Burdick, S., van der Hilst, R. D., Vernon, F. L., Martynov, V., Cox, T., Eakins, J., Karasu, G. H., Tylell, J., Astiz, L., and Pavlis, G. L. (2010). Model update january 2010: Upper mantle heterogeneity beneath north america from traveltime tomography with global and usarray transportable array data. *Seismological Research Letters*, 81(5):689–693.

Chen, T. and Clayton, R. W. (2009). Seismic attenuation structure in central mexico: Image of a focused high-attenuation zone in the mantle wedge. *Journal of Geophysical Research: Solid Earth (1978–2012)*, 114(B7).

Contreras-Reyes, E., Jara, J., Grevemeyer, I., Ruiz, S., and Carrizo, D. (2012). Abrupt change in the dip of the subducting plate beneath north chile. *Nature Geoscience*, 5(5):342–345.

Draganov, D., Wapenaar, K., and Thorbecke, J. (2006). Seismic interferometry: Reconstructing the earth's reflection response. *Geophysics*, 71(4):SI61–SI70.

Dziewonski, A. M. and Anderson, D. L. (1981). Preliminary reference earth model. *Physics of the earth and planetary interiors*, 25(4):297–356.

Hansen, P. C., Kilmer, M. E., and Høj, R. (2006). Exploiting residual information in the parameter choice for discrete ill-posed problems. *BIT Numerical Mathematics*, 46(1):41–59.

Husker, A. and Davis, P. M. (2009). Tomography and thermal state of the cocos plate subduction beneath mexico city. *Journal of Geophysical Research: Solid Earth (1978–2012)*, 114(B4).

Kennett, B. (1991). The removal of free surface interactions from three-component seismograms. *Geophysical Journal International*, 104(1):153–154.

Kennett, B., Engdahl, E., and Buland, R. (1995). Constraints on seismic velocities in the earth from traveltimes. *Geophysical Journal International*, 122(1):108–124.

Melo, G. and Malcolm, A. (2011). Microquake seismic interferometry with svd-enhanced green's function recovery. *The Leading Edge*, 30(5):556–562.

Payero, J. S., Kostoglodov, V., Shapiro, N., Mikumo, T., Iglesias, A., Pérez-Campos, X., and Clayton, R. W. (2008). Nonvolcanic tremor observed in the mexican subduction zone. *Geophysical Research Letters*, 35(7).

Pérez-Campos, X., Kim, Y. H., Husker, A., Davis, P. M., Clayton, R. W., Iglesias, A., Pacheco, J. F., Singh, S. K., Manea, V. C., and Gurnis, M. (2008). Horizontal subduction and truncation of the cocos plate beneath central mexico. *Geophysical Research Letters*, 35(18):L18303.

Ramírez-Herrera, M., Cundy, A., Kostoglodov, V., and Ortiz, M. (2009). Late holocene tectonic land-level changes and tsunamis at mitla lagoon, guerrero, mexico. *Geofísica internacional*, 48(2):195–209.

Ruigrok, E., Campman, X., Draganov, D., and Wapenaar, K. (2010). High-resolution lithospheric imaging with seismic interferometry. *Geophysical Journal International*, 183(1):339–357.

Snieder, R. (2004). Extracting the greens function from the correlation of coda waves: A derivation based on stationary phase. *Physical Review E*, 69(4):046610.

Stein, S. and Wysession, M. (2009). *An introduction to seismology, earthquakes, and earth structure*. Wiley-Blackwell.

Stubailo, I., Beghein, C., and Davis, P. (2012). Structure and anisotropy of the mexico subduction zone based on rayleigh-wave analysis and implications for the geometry of the trans-mexican volcanic belt. *Journal of Geophysical Research: Solid Earth (1978–2012)*, 117(B5).

Thorbecke, J. W. and Draganov, D. (2011). Finite-difference modeling experiments for seismic interferometry. *Geophysics*, 76(6):H1–H18.

Wapenaar, K., Draganov, D., Snieder, R., Campman, X., and Verdel, A. (2010). Tutorial on seismic interferometry: Part 1: Basic principles and applications. *Geophysics*, 75(5):75A195–75A209.

Wapenaar, K. and Fokkema, J. (2006). Green's function representations for seismic interferometry. *Geophysics*, 71(4):SI33–SI46.

Yilmaz, Ö. (2001). *Seismic data analysis: processing, inversion, and interpretation of seismic data*. Number 10. SEG Books.